

Squark–anti-squark pair production at the LHC: the electroweak contribution

W. HOLLIK and E. MIRABELLA

*Max-Planck-Institut für Physik (Werner-Heisenberg-Institut)
Föhringer Ring 6, D-80805 München, Germany*

Abstract

We present the complete NLO electroweak contribution of $\mathcal{O}(\alpha_s^2\alpha)$ to the production of diagonal squark–anti-squark pairs in proton–proton collisions. Compared to the lowest-order $\mathcal{O}(\alpha_s\alpha + \alpha^2)$ electroweak terms, the NLO contributions are also significant. We discuss the LO and NLO electroweak effects in cross sections and distributions at the LHC for the production of squarks different from top squarks, in various supersymmetric benchmark scenarios. LO and NLO can add up to 10% in cross sections and 25% in distributions.

1 Introduction

The exploration of electroweak symmetry breaking will be one of the main tasks at the Large Hadron Collider (LHC). Experiments are expected to either verify the Higgs mechanism of the Standard Model (SM), or to detect signals of physics beyond the SM. The concept of supersymmetry [1,2] provides a promising alternative version of the Higgs mechanism where symmetry breaking occurs without introducing new scalar couplings that potentially can become strong, thus stabilizing the electroweak scale. The realization of supersymmetry in terms of the Minimal Supersymmetric Standard Model (MSSM) [3–5], has come up as the most promising extension of the SM, a predictive framework that allows to make precise predictions to be investigated by indirect and direct experimental studies. The indirect access through virtual effects in electroweak precision data [6] provides an overall fit [7,8] with a quality at least as good as in the SM, in specific observables like $g - 2$ of the muon [9,10] even better, and yields bounds on the light Higgs boson mass with less tension than in the SM [11–13].

If supersymmetry (SUSY) is realized at the TeV scale or below, it will be accessible to direct experimental studies at the LHC through the production of SUSY particles. In particular, colored particles like squarks and gluinos will be copiously produced, and the hadronic production of squark–anti-squark pairs is expected to play an important role for SUSY hunting. The cross section is in the range from 0.5 to 10 pb for masses of squarks and gluinos below 1 TeV and can be measured with a statistical uncertainty of the order of a few percent even in the low luminosity regime. Moreover, squark cascade decays into $q\tilde{\chi}_1^0$ lead to a signature with missing E_T plus jets and possibly leptons that is well suited to detect MSSM signals [14,15]. The number of hard jets allows the distinction between gluino and squark decays. Finally with the help of decay chains one can reconstruct the mass of the squarks up to 2 TeV with a resolution better than 10 % [16–18].

The first prediction of the cross section for hadronic production of squark pairs in the early 1980's was done at lowest order $\mathcal{O}(\alpha_s^2)$ in supersymmetric QCD [19–23]. QCD contributions at NLO, $\mathcal{O}(\alpha_s^3)$, for the processes $PP \rightarrow \tilde{Q}^a\tilde{Q}^{b*}X$, $PP \rightarrow \tilde{Q}^a\tilde{Q}^bX$ ($Q \neq t$) were calculated more than ten years later [24,25]. They increase the cross section by typically 20 to 30 %, and they substantially reduce the dependence on the factorization and renormalization scale. NLO QCD corrections to the production of top-squark pairs, performed in [26], are also positive and can increase the cross section by 40–50%.

Besides the QCD-based production mechanisms, there are also partonic processes of electroweak origin, like diagonal and non-diagonal squark pair production from $q\bar{q}$ annihilation [27, 28]. They proceed through s -channel photon and Z exchange, and also through neutralino/chargino exchange in the t -channel (if \tilde{Q} is different from \tilde{t}), yielding terms of $\mathcal{O}(\alpha^2)$ and $\mathcal{O}(\alpha_s\alpha)$. Due to interference between the tree-level QCD and electroweak amplitudes for $\tilde{Q} \neq \tilde{t}$, the electroweak contributions can also become sizable, reaching values up to 20% [27].

For reliable predictions, electroweak contributions at NLO have to be taken into account as well. In the case of top-squark pair production [29–31], they were found to be significant, with effects up to 20%. In general, NLO electroweak (EW) contributions consist of loop contributions to the tree-level amplitudes for $q\bar{q}$ annihilation and gluon fusion, together with real photon and gluon bremsstrahlung processes, yielding an involved structure of interference terms in $q\bar{q}$ annihilation. Moreover, photon–gluon induced parton processes also contribute owing to the non-zero photon distribution in the proton. In this paper we present the NLO electroweak contributions, of $\mathcal{O}(\alpha_s^2\alpha)$, to the production of diagonal squark–anti-squark pairs different from top- and bottom-squarks,

$$P P \rightarrow \tilde{Q}^a \tilde{Q}^{a*} X \quad (\tilde{Q} \neq \tilde{t}, \tilde{b}). \quad (1)$$

They show significant differences to top-squark production, based on the following peculiarities.

- In leading order $\mathcal{O}(\alpha_s^2)$, the squark pair $\tilde{Q}^a \tilde{Q}^{a*}$ can be produced via annihilation of a $Q \bar{Q}$ pair through amplitudes that involve also the exchange of a gluino in the t -channel, thus enhancing the relative weight of the annihilation channel in (1).
- Electroweak tree diagrams with t -channel neutralino and chargino exchange are part of the amplitudes for $Q \bar{Q} \rightarrow \tilde{Q}^a \tilde{Q}^{a*}$ and $Q' \bar{Q}' \rightarrow \tilde{Q}^a \tilde{Q}^{a*}$, where Q' is the isospin partner of Q in a quark doublet, yielding EW–QCD interference already at the tree-level.
- At $\mathcal{O}(\alpha_s^2\alpha)$ many types of interferences occur between amplitudes of $\mathcal{O}(\alpha_s\alpha)$ and $\mathcal{O}(\alpha_s)$ as well as between $\mathcal{O}(\alpha_s^2)$ and $\mathcal{O}(\alpha)$ amplitudes.

These features make the calculation of the EW contributions of $\mathcal{O}(\alpha_s^2\alpha)$ to the processes (1) more involved than in the case of $\tilde{t}\tilde{t}^*$ production where no t -channel diagrams occur at lowest order. Our analysis shows that the EW effects of NLO can reach the same size as the tree-level EW contributions of $\mathcal{O}(\alpha_s\alpha)$ and $\mathcal{O}(\alpha^2)$, which we will include in our discussion as well.

The case of $\tilde{b}\tilde{b}^*$ production will not be treated here. Owing to b -tagging, bottom-squarks can be experimentally distinguished from the squarks of the first two generations [18, 32, 33]. Moreover, in the case of $\tilde{b}\tilde{b}^*$ production the partonic process $b\bar{b} \rightarrow \tilde{b}\tilde{b}^*$ exhibits specific features, like mixing between left- and right-handed b -squarks, mixing angle renormalization [34], non-negligible Higgs-boson contributions and enhanced Yukawa couplings for large values of $\tan\beta$ with the need of resummation [35]; other peculiarities for massive initial-state partons are the proper counting of the orders of the perturbative expansion [36, 37] and the appropriate choice of the factorization scale [38]. A dedicated extra analysis for b -squark final states thus seems appropriate.

The outline of the paper is as follows. In Section 2 we briefly summarize the various tree-level contributions to the processes (1). Section 3 describes the structure of the NLO terms of EW origin that contribute at $\mathcal{O}(\alpha_s^2\alpha)$ and the strategy of the calculation. Evaluation of the EW effects and their analysis for the LHC are presented in Section 4 and summarized in Section 5. A list of Feynman diagrams and counter terms with specification of renormalization, and technical details for the calculation of singular integrals are collected in the Appendix.

2 Tree-level contributions to squark pair production

In this section we list the lowest-order cross sections for the process (1) arising from tree-level amplitudes at order $\mathcal{O}(\alpha_s^2)$, $\mathcal{O}(\alpha_s\alpha)$ and $\mathcal{O}(\alpha^2)$. We will use the convention $d\sigma_X^{a,b}$ to denote the cross section for a partonic process X at a given order $\mathcal{O}(\alpha_s^a\alpha^b)$ in the strong and electroweak coupling constants. The parton luminosities for getting to the hadronic cross section are given by the convolution

$$\frac{dL_{ij}}{d\tau}(\tau) = \frac{1}{1 + \delta_{ij}} \int_{\tau}^1 \frac{dx}{x} \left[f_i(x) f_j\left(\frac{\tau}{x}\right) + f_j(x) f_i\left(\frac{\tau}{x}\right) \right], \quad (2)$$

where $f_i(x)$ is the momentum distribution of the parton i in the proton (PDF).

2.1 Squark pair production at leading order

The leading-order contribution to the process (1) is QCD based, of $\mathcal{O}(\alpha_s^2)$. In the notation mentioned above, the differential cross section reads as follows,

$$d\sigma_{PP \rightarrow \tilde{Q}^a \tilde{Q}^{a*}}^{\text{LO}}(S) = \sum_q \int_{\tau_0}^1 d\tau \frac{dL_{q\bar{q}}}{d\tau}(\tau) d\sigma_{q\bar{q} \rightarrow \tilde{Q}^a \tilde{Q}^{a*}}^{2,0}(s) + \int_{\tau_0}^1 d\tau \frac{dL_{gg}}{d\tau}(\tau) d\sigma_{gg \rightarrow \tilde{Q}^a \tilde{Q}^{a*}}^{2,0}(s). \quad (3)$$

The sum runs over the quarks $q = u, d, c, s$. S and $s = \tau S$ are the squared CM energies of the hadronic process (1) and of the partonic subprocess, respectively. Moreover, with the squark mass $m_{\tilde{Q},a}$, the threshold value τ_0 is determined by $\tau_0 = 4m_{\tilde{Q},a}^2/S$.

$d\sigma_{q\bar{q} \rightarrow \tilde{Q}^a \tilde{Q}^{a*}}^{2,0}$ and $d\sigma_{gg \rightarrow \tilde{Q}^a \tilde{Q}^{a*}}^{2,0}$ denote the $\mathcal{O}(\alpha_s^2)$ differential cross sections for the partonic processes

$$q(p_1) \bar{q}(p_2) \rightarrow \tilde{Q}^a(k_1) \tilde{Q}^{a*}(k_2), \quad (4)$$

$$g(p_1) g(p_2) \rightarrow \tilde{Q}^a(k_1) \tilde{Q}^{a*}(k_2), \quad (5)$$

respectively, which are obtained from the Feynman diagrams in Fig. 1 of Appendix A. Explicit expressions for these leading-order cross sections can be found in Refs. [19, 22, 23]. Owing to flavour conservation in SUSY QCD, the diagram with the exchange of a gluino in the t channel contributes only if $q = Q$.

2.2 Tree-level electroweak contributions of $\mathcal{O}(\alpha_s\alpha)$ and $\mathcal{O}(\alpha^2)$

The $\mathcal{O}(\alpha_s\alpha)$ and $\mathcal{O}(\alpha^2)$ contributions to the process (1), involving electroweak terms, can be written as follows,

$$d\sigma_{PP \rightarrow \tilde{Q}^a \tilde{Q}^{a*} X}^{\text{ew,LO}} = \sum_q \int_{\tau_0}^1 d\tau \left\{ \frac{dL_{q\bar{q}}}{d\tau}(\tau) \left(d\sigma_{q\bar{q} \rightarrow \tilde{Q}^a \tilde{Q}^{a*}}^{1,1} + d\sigma_{q\bar{q} \rightarrow \tilde{Q}^a \tilde{Q}^{a*}}^{0,2} \right) + \frac{dL_{\gamma g}}{d\tau}(\tau) d\sigma_{\gamma g \rightarrow \tilde{Q}^a \tilde{Q}^{a*}}^{1,1} \right\}. \quad (6)$$

The parton cross section $d\sigma_{q\bar{q} \rightarrow \tilde{Q}^a \tilde{Q}^{a*}}^{0,2}$ is obtained squaring the tree-level electroweak diagrams depicted in Fig. 2 of Appendix A. The diagram with t -channel neutralino exchange contributes only if $q = Q$, and the diagram with chargino exchange appears only if $q' = Q$, q' being the SU(2) partner of the quark q , since we treat the CKM matrix as unity. $d\sigma_{q\bar{q} \rightarrow \tilde{Q}^a \tilde{Q}^{a*}}^{1,1}$ originates from interference between the aforementioned tree-level electroweak diagrams and the tree-level QCD graphs of Fig. 1. Analytical expressions for these cross sections can be found in Ref. [27].

As a new element at $\mathcal{O}(\alpha_s\alpha)$, photon-gluon fusion occurs as a further partonic process,

$$\gamma(p_1) g(p_2) \rightarrow \tilde{Q}^a(k_1) \tilde{Q}^{a*}(k_2). \quad (7)$$

The corresponding cross section, with $t = (p_1 - k_1)^2$,

$$d\sigma_{\gamma g \rightarrow \tilde{Q}^a \tilde{Q}^{a*}}^{1,1} = \frac{dt}{16\pi s^2} \overline{\sum} |\mathcal{M}_{\gamma g \rightarrow \tilde{Q}^a \tilde{Q}^{a*}}^0|^2, \quad (8)$$

contains the spin- and color-averaged squared tree-amplitudes from the diagrams in Fig. A,

$$\overline{\sum} |\mathcal{M}_{\gamma g \rightarrow \tilde{Q}^a \tilde{Q}^{a*}}^0|^2 = 16\pi^2 \alpha \alpha_s e_{\tilde{Q}} \frac{m_{\tilde{Q},a}^4 (m_{\tilde{Q},a}^4 + s^2) + tu(tu - 2m_{\tilde{Q},a}^4)}{(t - m_{\tilde{Q},a}^2)^2 (u - m_{\tilde{Q},a}^2)^2}$$

with $u = (p_1 - k_2)^2$, and the electric charge $e_{\tilde{Q}}$ of the squark \tilde{Q} . The presence of photons in the proton follows from including NLO QED effects in the evolution equations for the PDFs. The photon PDF is part of the publicly available PDF set of [39]; together with the gluon PDF, the γg luminosity entering (6) is built according to Eq. (2).

3 Virtual and real $\mathcal{O}(\alpha_s^2 \alpha)$ corrections

In this section we describe the computation of the $\mathcal{O}(\alpha_s^2 \alpha)$ corrections to the process (1) arising from loops and from photon/gluon bremsstrahlung. The corresponding contributions to the hadronic cross section are expressed in obvious notation,

$$\begin{aligned} d\sigma_{PP \rightarrow \tilde{Q}^a \tilde{Q}^{a*} X}^{\text{ew,NLO}} &= \int_{\tau_0}^1 d\tau \frac{dL_{gg}(\tau)}{d\tau} \left(d\sigma_{gg \rightarrow \tilde{Q}^a \tilde{Q}^{a*}}^{2,1} + d\sigma_{gg \rightarrow \tilde{Q}^a \tilde{Q}^{a*} \gamma}^{2,1} \right) \\ &+ \sum_q \left\{ \int_{\tau_0}^1 d\tau \frac{dL_{q\bar{q}}(\tau)}{d\tau} \left(d\sigma_{q\bar{q} \rightarrow \tilde{Q}^a \tilde{Q}^{a*}}^{2,1} + d\sigma_{q\bar{q} \rightarrow \tilde{Q}^a \tilde{Q}^{a*} \gamma}^{2,1} + d\sigma_{q\bar{q} \rightarrow \tilde{Q}^a \tilde{Q}^{a*} g}^{2,1} \right) \right. \\ &\left. + \int_{\tau_0}^1 d\tau \left[\frac{dL_{qg}(\tau)}{d\tau} d\sigma_{qg \rightarrow \tilde{Q}^a \tilde{Q}^{a*} q}^{2,1} + \frac{dL_{\bar{q}g}(\tau)}{d\tau} d\sigma_{\bar{q}g \rightarrow \tilde{Q}^a \tilde{Q}^{a*} \bar{q}}^{2,1} \right] \right\}. \end{aligned} \quad (9)$$

Other bremsstrahlung contributions to the hadronic cross section are of the type

$$\gamma(p_1) q(p_2) \rightarrow \tilde{Q}^a(k_1) \tilde{Q}^{a*}(k_2) q(k_3), \quad \gamma(p_1) \bar{q}(p_2) \rightarrow \tilde{Q}^a(k_1) \tilde{Q}^{a*}(k_2) \bar{q}(k_3). \quad (10)$$

We will not consider this class of processes here; they are further suppressed by an additional factor α_s with respect to process (7), and thus negligible.

Diagrams and corresponding amplitudes are generated using **FeynArts** [40, 41]. The algebraic treatment and numerical evaluation of loop integrals is performed with support of **FormCalc** and **LoopTools** [42, 43]. IR singularities are regularized by a small photon mass, while quark masses are kept as regulators for the collinear singularities.

3.1 Gluon fusion with electroweak loops

The first class of corrections entering Eq. (9) are the $\mathcal{O}(\alpha_s^2 \alpha)$ electroweak virtual contributions to gg fusion (5), given by the partonic cross section

$$d\sigma_{gg \rightarrow \tilde{Q}^a \tilde{Q}^{a*}}^{2,1} = \frac{dt}{16\pi s^2} \overline{\sum} 2 \Re \{ \mathcal{M}_{gg \rightarrow \tilde{Q}^a \tilde{Q}^{a*}}^0 \mathcal{M}_{gg \rightarrow \tilde{Q}^a \tilde{Q}^{a*}}^{1,\text{ew}} \}, \quad (11)$$

\mathcal{M}^0 is the tree level gg amplitude (Fig. 1), and $\mathcal{M}^{1,\text{ew}}$ is the one-loop amplitude with EW insertions in the QCD-based gg tree diagrams. These loop diagrams do not depend on the flavour of the final squark and thus they are identical to those listed in [30] for the particular case of $\tilde{Q} = \tilde{t}$. We therefore do not repeat them here.

In order to get rid of the UV divergences we have to include the proper counterterms for one-loop renormalization. Their explicit expressions in terms of the renormalization constants can be found in

Appendix B. In the case of the gluon-fusion subprocess we have to renormalize the squark sector only. We use the on-shell scheme [30, 34, 44], where the independent parameters for a squark isospin doublet¹ are chosen to be the masses of the two up-squarks, the mass of one of the two down-squarks, and the two mixing angles (which, however are irrelevant for the light-quark squarks where mixing can be neglected). The actual expressions for the renormalization constants are also given in Appendix B.

Notice that part of the virtual corrections to squark pair production are loop diagrams for the gluon-gluon- H^0 vertex, with the heavy neutral MSSM Higgs boson H^0 . These terms become resonant when $m_{H^0} \geq 2m_{\tilde{Q},a}$ and have to be considered a contribution to the process of H^0 production via gluon fusion with the subsequent decay $H^0 \rightarrow \tilde{Q}^a \tilde{Q}^{a*}$, rather than an electroweak loop correction. We will not consider scenarios in which such resonances occur.

3.2 Gluon fusion with real photon emission

The IR singularities arising from virtual photons in (11) are cancelled by including bremsstrahlung of real photons at $\mathcal{O}(\alpha_s^2 \alpha)$,

$$g(p_1) g(p_2) \rightarrow \tilde{Q}^a(k_1) \tilde{Q}^{a*}(k_2) \gamma(k_3), \quad (12)$$

according to the diagrams depicted in Fig. 4. The integral over the photon phase space is IR divergent in the soft-photon region, *i.e.* for $k_3^0 \rightarrow 0$, and cancels the corresponding virtual singularities when added to the virtual contributions according to Eq. (9).

For the technical treatment of photon-momentum integration and isolation of divergences we apply two different procedures: the methods of dipole subtraction and of phase space slicing. In the dipole subtraction approach, one has to add and subtract an auxiliary function to the differential cross section that matches pointwise the singularities and is easy enough to be integrated analytically; the integral over the subtracted cross section is convergent and can be done numerically. Due to the universality of the soft singularities general expressions for these functions are available. In particular we use the expressions given in Ref. [45]. Although the formulae quoted in this reference apply to processes involving fermions only, they can be generalized to processes with charged bosons owing to the universal structure of the IR singularities.

The phase space slicing technique restricts the phase space integration to the region with a minimum photon energy $\Delta E = \delta_s \sqrt{s}/2$. The integration over this region is thus convergent and can be performed numerically. The complementary integral over the singular region with $k_3 < \Delta E$ can be done analytically in the eikonal approximation [46], which is a good approximation if the cut δ_s is sufficiently small. More details are given in Appendix C. Comparison between the two methods provides a non trivial check of the computation. As illustrated in Fig. 12, the two methods yield results which are in good numerical agreement.

3.3 $q\bar{q}$ annihilation with electroweak and QCD loops

The structure of the parton processes of $q\bar{q}$ annihilation at higher order is more involved and requires a simultaneous treatment of electroweak and QCD loops. The virtual contributions of one-loop order to the partonic cross section is given by the interference of tree-level and loop amplitudes,

$$d\sigma_{q\bar{q} \rightarrow \tilde{Q}^a \tilde{Q}^{a*}}^{2,1} = \frac{dt}{16\pi s^2} \overline{\sum} \left\{ 2 \Re \{ \mathcal{M}_{q\bar{q} \rightarrow \tilde{Q}^a \tilde{Q}^{a*}}^{0,\text{qcd}*} \mathcal{M}_{q\bar{q} \rightarrow \tilde{Q}^a \tilde{Q}^{a*}}^{1,\text{ew}} \} + 2 \Re \{ \mathcal{M}_{q\bar{q} \rightarrow \tilde{Q}^a \tilde{Q}^{a*}}^{0,\text{ew}*} \mathcal{M}_{q\bar{q} \rightarrow \tilde{Q}^a \tilde{Q}^{a*}}^{1,\text{qcd}} \} \right\}, \quad (13)$$

where $\mathcal{M}^{0,\text{qcd}}$ ($\mathcal{M}^{0,\text{ew}}$) is the amplitude related to the tree-level QCD (EW) diagrams depicted in Fig. 1 (2). $\mathcal{M}^{1,\text{ew}}$ is the one-loop amplitude arising from the EW corrections to the QCD tree-level diagrams and the

¹Due to SU(2) invariance, mass renormalization of the different squarks from the same SU(2) doublet is correlated and has to be performed simultaneously.

QCD corrections to the EW tree-level diagrams. Finally, $\mathcal{M}^{1,\text{qed}}$ is the one-loop amplitude corresponding to the QCD corrections to the QCD tree-level diagrams.

The diagrams entering $\mathcal{M}^{1,\text{ew}}$ are displayed in Figs. 5–7 of Appendix A. They also contain the diagrams with counterterm insertions required for renormalization and cancellation of UV divergences. The counterterms and the necessary renormalization constants can be found in Appendix B. Besides squark renormalization, also quark renormalization is needed.

$\mathcal{M}^{1,\text{qed}}$ can be obtained from the Feynman diagrams in Fig. 8 of Appendix A, including the proper counterterms. Besides renormalization of the squark sector, we have to renormalize also the gluino mass, the strong coupling g_s , and the quark–squark–gluino coupling \hat{g}_s , which is related to g_s via supersymmetry. The strong coupling constant is renormalized in the $\overline{\text{MS}}$ scheme, modified according to Ref. [24] in order to decouple heavy particles (top, gluino, squarks) from the running of α_s . For the non-standard loop contributions, this procedure is equivalent to the “zero-momentum subtraction” used in Ref. [47]. Since dimensional regularization violates supersymmetry in higher orders, a finite difference between \hat{g}_s and g_s is encountered at one-loop order. Supersymmetry is restored by shifting the renormalization constant for \hat{g}_s by the corresponding finite amount, which means an unsymmetric renormalization of \hat{g}_s and g_s . More details and the specification of the counterterms can be found in Appendix B.

3.4 $q\bar{q}$ annihilation with real photon emission

The diagrams in Fig. 9 of Appendix A constitute the generic amplitude for photon bremsstrahlung at $\mathcal{O}(\alpha_s^2\alpha)$ in the $q\bar{q}$ annihilation channel,

$$q(p_1) \bar{q}(p_2) \rightarrow \tilde{Q}^a(k_1) \tilde{Q}^{a*}(k_2) \gamma(k_3). \quad (14)$$

The corresponding cross section is singular both in the IR soft-photon region and in the collinear region (*e.g.* whenever $k_3 p_i \rightarrow 0$). Although IR singularities cancel in sufficiently inclusive observables, collinear singularities from initial-state radiation remain and have to be absorbed via factorization in the PDFs.

The extraction of the singularities has been performed using the two different methods described in section 3.2. In phase space slicing, in this case, we have to introduce a further collinear cutoff δ_c on the angle between the photon and the radiating quark/antiquark. For sufficiently small δ_c , the integral over the singular region can be performed analytically. Explicit expressions can be found in Appendix C. In Fig. 12 we visualize the comparison between the two methods in the specific case of the partonic process $u\bar{u} \rightarrow \tilde{u}^L \tilde{u}^{L*} \gamma$ as an example.

3.5 $q\bar{q}$ annihilation with real gluon emission

Finally, we have to take into account the class of $q\bar{q}$ annihilation processes with real gluon bremsstrahlung,

$$q(p_1) \bar{q}(p_2) \rightarrow \tilde{Q}^a(k_1) \tilde{Q}^{a*}(k_2) g(k_3), \quad (15)$$

from either EW-based (Fig. 10 a) or QCD-based Born diagrams (Fig. 10 b). This class contributes to the cross section at $\mathcal{O}(\alpha_s^2\alpha)$ through interference between the graphs of Fig. 10 a and Fig. 10 b. The cross section exhibits singularities when the gluon becomes soft or collinear to the initial-state quark/antiquark. The soft singularities cancel against those from the virtual photon/gluon contributions in $q\bar{q}$ annihilation, when added along Eq. (9), while remaining collinear singularities have to be absorbed in the PDFs by factorization. IR and collinear singularities can be treated by mass regularization.

For applying the phase space slicing method, the eikonal current has to be modified due to colour correlations after the emission of the soft gluon (see Refs. [48–50] and Appendix C for details). Colour correlation has to be taken into account also when using the Dipole Subtraction Method; we modified the formulae of Ref. [45] accordingly, following the guidelines of Ref. [48]. In Fig. 12 we illustrate the comparison between the two methods also for gluon radiation, with good numerical agreement.

3.6 $q(\bar{q})g$ fusion

A last class of partonic processes at the considered order is given by (anti-)quark-gluon fusion,

$$\begin{aligned} q(p_1) g(p_2) &\rightarrow \tilde{Q}^a(k_1) \tilde{Q}^{a*}(k_2) q(k_3), \\ \bar{q}(p_1) g(p_2) &\rightarrow \tilde{Q}^a(k_1) \tilde{Q}^{a*}(k_2) \bar{q}(k_3). \end{aligned} \quad (16)$$

This IR finite class contributes at $\mathcal{O}(\alpha_s^2\alpha)$ through the interference between the diagrams of Fig. 11 a and Fig. 11 b. Mass singularities arise when the incoming gluon and outgoing (anti-)quark are collinear. These collinear divergences are again absorbed into the PDFs. Their extraction has been performed using the two methods described above in section 3.2. Explicit expressions for the cross section in the collinear region can be found in Appendix C. The actual expression of the subtraction function used in the Dipole Subtraction method is obtained from the formulae in Ref. [51]. Since those formulae are given there for the case of photon–quark splitting we have to consistently redo the color algebra. In Fig. 12 we show the agreement between the two methods for the example $ug \rightarrow \tilde{u}^L \tilde{u}^{L*} u$.

In specific cases of SUSY parameters, when kinematically allowed, the internal-state gauginos can be on-shell. The poles are regularized by introducing the width of the corresponding gluino, neutralino, or chargino. Potential problems related to gauge invariance [52] do not occur here.

3.7 Factorization of initial-state collinear singularities

The $\mathcal{O}(\alpha_s^2\alpha)$ corrections to partonic cross sections contain universal initial-state collinear singularities that can be absorbed into the PDFs choosing a factorization scheme where singularities of relative order $\mathcal{O}(\alpha)$, the lowest order PDF $f_i(x)$ for parton i ($= q, \bar{q}$) is related to the experimentally accessible distribution $f_i(x, \mu_F)$ via [53, 54]

$$\begin{aligned} f_i(x) &= f_i(x, \mu_F) \left\{ 1 + \frac{\alpha e_i^2 + \alpha_s C_F}{\pi} \left[-1 + \ln \delta_s + \ln^2 \delta_s + \left(\ln \delta_s + \frac{3}{4} \right) \ln \left(\frac{m_i^2}{\mu_F^2} \right) \right] + \frac{1}{4} \frac{\alpha e_i^2}{\pi} h(\delta_s) \right\} \\ &+ \int_x^{1-\delta_s} \frac{dz}{z} f_i \left(\frac{x}{z}, \mu_F \right) \left\{ P_{ii}(z) \frac{\alpha e_i^2 + C_F \alpha_s}{2\pi} \left[\ln \left(\frac{m_i^2 (1-z)^2}{\mu_F^2} \right) + 1 \right] - \frac{\alpha e_i^2}{2\pi} H(z) \right\} \\ &+ \int_x^1 \frac{dz}{z} f_g \left(\frac{x}{z}, \mu_F \right) P_{ig}(z) \frac{\alpha_s T_F}{2\pi} \ln \left(\frac{m_i^2}{\mu_F^2} \right), \end{aligned} \quad (17)$$

with the factorization scale μ_F , $C_F = \frac{4}{3}$, $T_F = \frac{1}{2}$ and the electric charge e_i . The splitting functions P_{ii} , P_{ig} are defined in the usual way,

$$P_{ii}(z) = \frac{1+z^2}{1-z} \quad P_{ig}(z) = z^2 + (1-z)^2, \quad (18)$$

and the functions h and H are given by

$$h(\delta_s) = 9 + \frac{2\pi^2}{3} + 3 \ln \delta_s - 2 \ln^2 \delta_s, \quad H(z) = P_{ii}(z) \ln \left(\frac{1-z}{z} \right) - \frac{3}{2} \frac{1}{1-z} + 2z + 3. \quad (19)$$

The actual effect of the factorization of the initial collinear singularities is to substitute $f_i(x)$ by $f_i(x, \mu_F)$ in the definition of the quark–antiquark luminosity (2) and thus to obtain a further $\mathcal{O}(\alpha_s^2\alpha)$ contribution to be added to Eq. (9). This contribution reads:

$$\begin{aligned} &\sum_q \int_{\tau_0}^1 d\tau \frac{dL_{q\bar{q}}}{d\tau}(\tau) \left\{ \left(\frac{2\alpha e_q^2}{\pi} \kappa_q^{\text{soft}} + \frac{\alpha e_q^2}{2\pi} h(\delta_s) \right) d\sigma_{q\bar{q} \rightarrow \tilde{Q}^a \tilde{Q}^{a*}}^{2,0}(s) + \frac{2\alpha_s C_F}{\pi} \kappa_q^{\text{soft}} d\sigma_{q\bar{q} \rightarrow \tilde{Q}^a \tilde{Q}^{a*}}^{1,1}(s) \right. \\ &+ \left. \int_{x_0}^{1-\delta_s} dz \left[\left(\frac{\alpha e_q^2}{\pi} \kappa_q^{\text{coll}}(z) - \frac{\alpha e_q^2}{\pi} H(z) \right) d\sigma_{q\bar{q} \rightarrow \tilde{Q}^a \tilde{Q}^{a*}}^{2,0}(zs) + \frac{\alpha_s C_F}{\pi} \kappa_q^{\text{coll}}(z) d\sigma_{q\bar{q} \rightarrow \tilde{Q}^a \tilde{Q}^{a*}}^{1,1}(zs) \right] \right\} \\ &+ \sum_q \int_{\tau_0}^1 d\tau \left[\left(\frac{dL_{qg}}{d\tau}(\tau) + \frac{dL_{\bar{q}g}}{d\tau}(\tau) \right) \int_{x_0}^1 dz P_{qg}(z) \frac{\alpha_s T_F}{2\pi} \ln \left(\frac{m_q^2}{\mu_F^2} \right) d\sigma_{q\bar{q} \rightarrow \tilde{Q}^a \tilde{Q}^{a*}}^{1,1}(zs) \right], \end{aligned} \quad (20)$$

parameter	SPS1a'	SPS5	SU1	SU4
$M_{1/2}$	250 GeV	300 GeV	350 GeV	160 GeV
M_0	70 GeV	150 GeV	70 GeV	200 GeV
A_0	-300 GeV	-1000 GeV	0	-400 GeV
$\text{sign}(\mu)$	+	+	+	+
$\tan\beta(M_Z)$	10.37	5	10	10

Table 1: Input parameters in the four benchmark scenarios.

where $x_0 = (4m_{\tilde{Q},a}^2)/s$, while κ_q^{soft} and $\kappa_q^{\text{coll}}(z)$ are defined as

$$\begin{aligned}\kappa_q^{\text{soft}} &= \ln\delta_s + \ln^2\delta_s + \left(\ln\delta_s + \frac{3}{4}\right) \ln\left(\frac{m_q^2}{\mu_F^2}\right) - 1, \\ \kappa_q^{\text{coll}}(z) &= P_{qq}(z) \left[\ln\left(\frac{m_q^2(1-z)^2}{\mu_F^2}\right) + 1 \right].\end{aligned}\tag{21}$$

The singularities in $\kappa_q^{\text{coll}}(z)$ cancel in the sum of the real corrections and of the contribution (20), as can be easily checked using the analytic expressions of $d\sigma_{q\bar{q}\rightarrow\tilde{Q}^a\tilde{Q}^{a*}\gamma}^{2,1}$ and $d\sigma_{q\bar{q}\rightarrow\tilde{Q}^a\tilde{Q}^{a*}g}^{2,1}$ in the collinear regions [see Eqs. (39) and (43) of Appendix C]. The remaining singularities of the real corrections are exactly cancelled against those in κ_q^{soft} and in the virtual corrections. The mass singularities in the last line of Eq. (20) are cancelled by those of $d\sigma_{qg\rightarrow\tilde{Q}^a\tilde{Q}^{a*}q}^{2,1}$ and $d\sigma_{qg\rightarrow\tilde{Q}^a\tilde{Q}^{a*}\bar{q}}^{2,1}$, as can be inferred from their analytic expressions in the collinear region [Eq. (45) of Appendix C].

For the calculation of hadronic observables we use the MRST2004qed parton distribution functions [39]. Factorization and renormalization scales are chosen as equal, $\mu_R = \mu_F = m_{\tilde{Q},a}$.

4 Numerical Analysis

For the numerical evaluation and for illustration of the EW effects, we choose four different benchmark scenarios: the point SPS1a' suggested by the SPA convention [55], the snowmass point SPS5 [56] characterized by light stops, and two of the points chosen for detector simulation in the ATLAS ‘‘Computing System Commissioning’’ exercise [57]: the point SU1 in the coannihilation region, and the point SU4 characterized by light SUSY particles. The input parameters $M_{1/2}$, M_0 , A_0 , defined at the GUT scale, and $\tan\beta$ are put together in Table 1. The MSSM input for the actual calculation is obtained with the help of the program `SPheno` [58], together with the program `SuSpect` [59] as a cross check. The pole masses of the squarks of the first generation obtained with the two different codes are shown in Table 2. Since the quarks of the first two generations are treated as massless, same-chirality and same-isospin squarks are degenerate, therefore we do not show the masses of the squarks belonging to the second generation. The difference between the masses provided by the two codes is below 1%. The different inputs given by the two codes give rise to a differences in the total cross section of the order of 2 – 3%. The standard model parameters are taken from Ref. [60].

We introduce the following conventions:

- We will refer to the sum of $\mathcal{O}(\alpha_s\alpha)$, $\mathcal{O}(\alpha^2)$ and $\mathcal{O}(\alpha_s^2\alpha)$ contributions as ‘‘the EW contribution’’.
- We will use the quantity δ to denote the relative EW contribution, defined as $\delta = (\mathcal{O}_{\text{NLO}} - \mathcal{O}_{\text{LO}})/\mathcal{O}_{\text{LO}}$, where \mathcal{O} is a generic observable and \mathcal{O}_{NLO} is the sum of the LO in Eq. (3) and the EW contribution.

	SPS1a'	SPS5	SU1	SU4
$m_{\tilde{u},R}$	548.1 (545.6)	660.3 (657.4)	739.7 (736.3)	412.6 (411.2)
$m_{\tilde{u},L}$	565.3 (562.0)	681.5 (677.5)	765.6 (760.7)	420.3 (418.6)
$m_{\tilde{d},R}$	547.9 (545.4)	659.2 (656.9)	738.0 (734.6)	413.9 (412.5)
$m_{\tilde{d},L}$	570.7 (567.5)	685.5 (681.8)	769.6 (764.7)	427.5 (425.8)

Table 2: Pole masses (in GeV) of the squarks of the first generation in the various SUSY scenarios. They are obtained using `SPheno` [58]; those computed with `SuSpect` [59] are quoted inside the brackets for comparison.

4.1 Different squark species

Electroweak interactions depend on the hypercharge of the squarks, hence the production cross sections are flavour and chirality dependent. In this subsection we will study the production of four squark species, focusing on the SPS1a' point. Since the masses of the light quarks can be neglected, the weak eigenstates of the squarks are also the mass eigenstates; thus, in the following, the two squarks of a given flavour are distinguished by means of their chiralities, $\tilde{Q}^a = \tilde{Q}^L, \tilde{Q}^R$.

Dependence on squark flavour and chirality

In Tab. 3 we show the integrated hadronic cross section for the diagonal pair production of $\tilde{u}^L, \tilde{u}^R, \tilde{d}^L$ and \tilde{c}^L . In the case of the production of the squarks of the first generation there is a cancellation between $\mathcal{O}(\alpha_s\alpha)$ and $\mathcal{O}(\alpha^2)$ contributions. The overall $\mathcal{O}(\alpha_s\alpha + \alpha^2)$ correction is negative and of the same order of magnitude as the $\mathcal{O}(\alpha_s^2\alpha)$ one. Since they have the same sign their effect is enhanced. In the case of \tilde{c}^L production the situation is different: $\mathcal{O}(\alpha_s\alpha)$, $\mathcal{O}(\alpha^2)$, and $\mathcal{O}(\alpha_s^2\alpha)$ corrections are positive, $\mathcal{O}(\alpha_s^2\alpha)$ contribution being the most important ones (see also the discussion below).

As a general remark, the EW effects are always larger for left-handed squarks. For a given chirality and generation, the EW contributions are more important in the case of up-type squarks. For comparison we also estimate the corresponding NLO QCD corrections using the code `PROSPINO` [25]; they are positive, weakly dependent on the flavour of the produced squarks, and of the order of 47 – 48%.

Fig. 13 shows the relative EW contribution (right part) in the “cumulative invariant mass distribution” $\sigma(M_{\text{inv}})$, that is the cross section integrated up to the value M_{inv} of the squark–antisquark invariant mass. A common feature is that in the low invariant mass region the NLO EW contribution is positive, rather steeply decreasing as the invariant mass increases, reaching the plateau at $M_{\text{inv}} \geq 2000$ GeV which corresponds to the total cross section. The left part of Fig. 13 shows the relative size of the individual contributions arising from the various channels. The contribution from the gluon fusion channel is always positive and dominates at lower values of M_{inv} , whereas the $q\bar{q}$ annihilation channel part is negative. Looking at the relative contributions of the different channels in the high invariant mass region, which corresponds to the total cross section, one can understand the origin of the different behaviour of the NLO EW corrections in the case of $u^L u^{L*}$ and $c^L c^{L*}$ production. For up-squark pairs, the $\mathcal{O}(\alpha_s\alpha)$ and $\mathcal{O}(\alpha_s^2\alpha)$ terms are dominated by the $q\bar{q}$ annihilation channels, which yield a negative contribution; for charm-squark production, however, the $\mathcal{O}(\alpha_s\alpha)$ [$\mathcal{O}(\alpha_s^2\alpha)$] corrections are dominated by the $q\gamma$ fusion [gg fusion] channel and thus positive. This shows the key role played by the partonic processes $Q\bar{Q}, Q'\bar{Q}' \rightarrow \tilde{Q}^a\tilde{Q}^{a*}$, where Q and Q' belong to the same isospin doublet. Indeed, in the case of $u^L u^{L*}$ production their contribution is negative and the largest out of the $q\bar{q}$ annihilation channels. In $c^L c^{L*}$ production they are suppressed by the PDFs of the charm and strange quarks and hence the contributions

	$\tilde{u}^R \tilde{u}^{R*}$	$\tilde{u}^L \tilde{u}^{L*}$	$\tilde{d}^L \tilde{d}^{L*}$	$\tilde{c}^L \tilde{c}^{L*}$
$\mathcal{O}(\alpha_s^2)$	$(36.83 \pm 0.03) \cdot 10^{-2}$	$(31.31 \pm 0.01) \cdot 10^{-2}$	$(25.89 \pm 0.01) \cdot 10^{-2}$	$(22.65 \pm 0.01) \cdot 10^{-2}$
$\mathcal{O}(\alpha_s \alpha)$	$(-9.00 \pm 0.01) \cdot 10^{-3}$	$(-3.54 \pm 0.01) \cdot 10^{-2}$	$(-3.83 \pm 0.01) \cdot 10^{-2}$	$(2.82 \pm 0.01) \cdot 10^{-3}$
$\mathcal{O}(\alpha^2)$	$(2.42 \pm 0.01) \cdot 10^{-3}$	$(2.39 \pm 0.01) \cdot 10^{-2}$	$(3.20 \pm 0.01) \cdot 10^{-2}$	$(2.11 \pm 0.01) \cdot 10^{-3}$
$\mathcal{O}(\alpha_s^2 \alpha)$	$(-3.09 \pm 0.05) \cdot 10^{-3}$	$(-1.05 \pm 0.01) \cdot 10^{-2}$	$(-7.82 \pm 0.07) \cdot 10^{-3}$	$(5.89 \pm 0.01) \cdot 10^{-3}$
$\delta(\%)$	-2.6	-7.0	-5.5	4.8

Table 3: Total cross section for the diagonal pair production of different squark species in the SPS1a' scenario. Beside the LO contribution, of $\mathcal{O}(\alpha_s^2)$, we show the yields of the different orders contributing to the NLO EW corrections. Cross sections are given in pb. δ is defined according to Sec. 4.

from the $q\bar{q}$ annihilation channels are negligible. As a result the overall contribution to total cross section is negative at the level of 5% for the left-handed up-squarks, while for the left-handed charm-squarks it is of the same order of magnitude but positive.

The contribution of the $g\gamma$ channel is independent on the squark chirality, determined only by the electric charge of the produced squarks, which makes the $g\gamma$ channel contribution for up-squark pair production four times bigger than that for down-squarks. Owing to the mass degeneracy between same-chirality and same-isospin squarks the gg fusion channel is independent on the generation of the produced squark.

The invariant mass distribution itself is displayed in Fig. 14 for the various squark species, showing also the breakdown into the individual channels. For each squark species, the EW contributions are positive in the low invariant mass region and become negative for larger values of M_{inv} , reaching the level of 15% for \tilde{u}^L squarks.

Fig. 15 contains the transverse momentum distribution of the squarks. Again, the EW effects are more pronounced for left-handed chirality yielding more than 30% negative contributions for large p_T . As new feature, the LO EW contribution can be positive for low p_T , especially for the \tilde{d}^L case, originating from the PDF-enhanced parton process $u\bar{u} \rightarrow \tilde{d}^L \tilde{d}^{L*}$ through t -channel chargino exchange. This positive part is practically compensated by the NLO $\mathcal{O}(\alpha_s^2 \alpha)$ contributions in the $q\bar{q}$ annihilation channel.

Dependence on the squark masses

To study the dependence of the NLO EW contributions on the mass of the squarks, we vary $m_{\tilde{u},R}$, setting $m_{\tilde{d},R} = m_{\tilde{u},R}$ and $m_{\tilde{u},L} = m_{\tilde{u},L}(1 + \varepsilon)$ with $\varepsilon = 0.03$, which is the value at the SPS1a' point. The values are also taken for the other generations as well as for the sleptons. The other parameters are kept as in SPS1a'. Each parameter point was checked to satisfy the bounds on SUSY particles from LEP [61, 62] and Tevatron [63], and the bound on the mass of the light Higgs boson h^0 , which has been computed using FeynHiggs 2.5.1 [64–66]. Moreover, each point fullfills the condition $|\Delta\rho| < 0.025$, where $\Delta\rho$ is the dominant squark contribution to the electroweak ρ parameter.

The relative EW contributions are shown in Fig. 16 for the total cross section, for each of the various squark types. The quantity ξ displayed in the right panel is the fraction of each the gg fusion and the $q\bar{q}$ annihilation channel in the total cross section, at leading order $\mathcal{O}(\alpha_s^2)$. The $q\bar{q}$ channel becomes more and more important as $m_{\tilde{u},R}$ increases. This feature, already pointed out in Ref. [19], is a consequence of the t -channel gluino exchange diagrams. The increasing importance of $q\bar{q}$ annihilation allows a better understanding of the particular role of the NLO corrections to the $q\bar{q}$ channel with increasing squark

	SPS5	SU1	SU4
$\mathcal{O}(\alpha_s^2)$	$(10.62 \pm 0.01) \cdot 10^{-2}$	$(51.77 \pm 0.02) \cdot 10^{-3}$	$(16.14 \pm 0.01) \cdot 10^{-1}$
$\mathcal{O}(\alpha_s \alpha)$	$(-1.37 \pm 0.01) \cdot 10^{-2}$	$(-7.22 \pm 0.01) \cdot 10^{-3}$	$(-1.45 \pm 0.01) \cdot 10^{-1}$
$\mathcal{O}(\alpha^2)$	$(9.11 \pm 0.01) \cdot 10^{-3}$	$(4.73 \pm 0.01) \cdot 10^{-3}$	$(10.16 \pm 0.01) \cdot 10^{-2}$
$\mathcal{O}(\alpha_s^2 \alpha)$	$(-4.83 \pm 0.03) \cdot 10^{-3}$	$(-2.75 \pm 0.02) \cdot 10^{-3}$	$(-2.61 \pm 0.01) \cdot 10^{-2}$
$\delta(\%)$	-8.9	-10.1	-4.3

Table 4: Same as Tab. 3 but focusing on $\tilde{u}^L \tilde{u}^{L*}$ production in different SUSY scenarios.

masses. Especially for left-handed up- and down-squarks, the NLO EW contributions become more important than the LO ones, with effects of more than 20%. In the charm-squark production case $q\bar{q}$ channel is subleading with respect to the gg and $g\gamma$ fusion channels due to the aforementioned suppression of charm and strange PDFs. The total sum of the EW contributions is shown in the right panel of Fig. 16. For illustration, we also give an estimate of the formal statistical uncertainty $\delta_{\text{stat}} = (L \sigma^{\text{NLO}})^{-1/2}$, assuming a luminosity $L = 100 \text{ fb}^{-1}$.

4.2 Different SUSY scenarios

Here we discuss the electroweak effects in the different SUSY scenarios mentioned above. As a concrete example, we consider the production of \tilde{u}^L squarks, with the corresponding masses listed in Table 2.

In Table 4 we show the total cross section for the aforementioned production process. The LO contribution and the different orders entering the NLO EW corrections are shown separately. As one can see the absolute value of the different contributions decreases as the mass of $m_{\tilde{u},L}$ increases, while the relative yield of the NLO EW corrections increases with the mass of the produced squarks. In the case of the SU1 scenario NLO EW corrections are negative and of the order of 10%. The corresponding NLO QCD corrections are estimated using the code PROSPINO [25]; they are of the order of 45 – 50%.

Fig. 17 contains the cumulative invariant mass distribution, again with the individual and the total EW contributions, which show a similar behaviour for all the chosen scenarios. Also the differential invariant mass distribution, displayed in Fig. 18, has similar qualitative features in all scenarios. At low values, the gluon fusion part dominates and renders the total EW contribution positive. At larger values, the contributions from $q\bar{q}$ annihilation turn the EW contribution to the negative region; thereby the NLO part is always of about the same size as the LO part.

In Fig. 19 we show the transverse momentum distribution in the various cases. Again, their shape depends only weakly on the scenario.

This general situation is only slightly changed when kinematical cuts are imposed, as we find from repeating our analysis for an exemplary set of cuts on the transverse momentum and on the rapidity of the two squarks,

$$p_T > 150 \text{ GeV}, \quad |y| < 2.5.$$

The cut on the rapidity is not effective because the NLO EW contributions to the rapidity distribution are very small for $|y| > 2.5$. More important is the cut on the transverse momentum. It excludes the kinematical region where the largest part of the gluon channel contribution comes from. Moreover, this cut suppresses also the contribution of the $g\gamma$ channel and enhances the influence of the $q\bar{q}$ channel by excluding the region with a positive p_T distribution. As a result, the negative EW contribution to the

total cross section is larger than without cuts, as one can see from Fig. 20.

Dependence on the gluino mass

Finally we study the dependence of the EW contribution as a function of the mass of the gluino $m_{\tilde{g}}$, with the other parameters kept fixed according to the SPS1a' point. Again, the parameter range is in accordance with the phenomenological constraints described in the previous subsection 4.1. At LO, the gluon fusion channel does not depend on the gluino mass, while the $q\bar{q}$ annihilation channel contribution decreases with increasing $m_{\tilde{g}}$, as displayed in Fig. 21. In the low $m_{\tilde{g}}$ region the two channels contribute equally to the production cross section, while gluon fusion becomes dominant as the mass of the gluino increases. The relative EW contributions from the various channels are flat, adding up to a total EW contribution from -7 to -3% for gluino masses between 500 and 2000 GeV. Thereby, in $q\bar{q}$ annihilation, both the tree-level term $\mathcal{O}(\alpha_s\alpha + \alpha^2)$ and the NLO corrections $\mathcal{O}(\alpha_s^2\alpha)$, are practically of the same size.

5 Conclusions

We have computed the $\mathcal{O}(\alpha_s^2\alpha)$ NLO electroweak contributions to the production of flavour-diagonal squark–anti-squark pairs in proton–proton collisions, in combination with the electroweak LO tree-level contributions of $\mathcal{O}(\alpha_s\alpha + \alpha^2)$.

We have performed an explicit study of the electroweak contributions for each case of the four squark species in the first SU(2) doublet, with a numerical analysis for the LHC. The electroweak effects can give rise to sizeable modifications in cross sections and distributions, in particular for left-handed squarks. Thereby, the NLO terms are significant and have to be considered together with the tree-level contributions. They show a strong dependence on the squark masses, increasing their relative influence with the mass of the squarks.

Moreover, we have investigated several SUSY benchmark scenarios and found that the behaviour of the electroweak contributions is only weakly dependent on the scenario. Also the gluino-mass dependence is weak. In summary, the electroweak contributions in squark-pair production can reach 20–25% in size and are thus significant; about half is carried by the NLO contributions. As a final remark we would like to mention that the NNLO QCD contributions, of $\mathcal{O}(\alpha_s^4)$, can be expected to be of similar size.

Acknowledgments

We thank Stefan Dittmaier and Stefano Pozzorini for useful discussions, and Maike Trenkel for cross checking part of the results.

Appendix

A Feynman diagrams

In this Appendix generic diagrams for the various contributions to the different channels are shown. We choose the up-squark case as a specific example. In the following we will use the label S^0 (S) to denote all the neutral (charged) Higgs bosons, while $V^0 = \gamma, Z$.

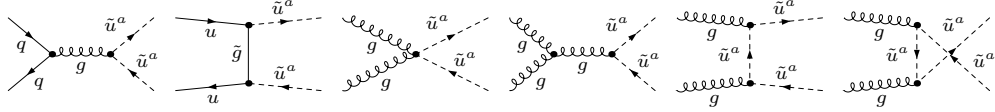


Figure 1: Tree-level QCD diagrams for $q\bar{q} \rightarrow \tilde{u}^a \tilde{u}^{a*}$ and for $gg \rightarrow \tilde{u}^a \tilde{u}^{a*}$.

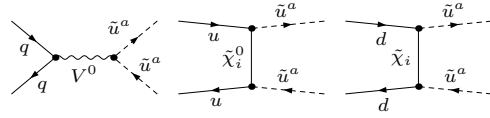


Figure 2: Tree-level EW diagrams for $q\bar{q} \rightarrow \tilde{u}^a \tilde{u}^{a*}$.

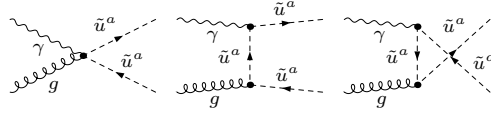


Figure 3: Lowest-order diagrams for photon-gluon fusion $\gamma g \rightarrow \tilde{u}^a \tilde{u}^{a*}$.

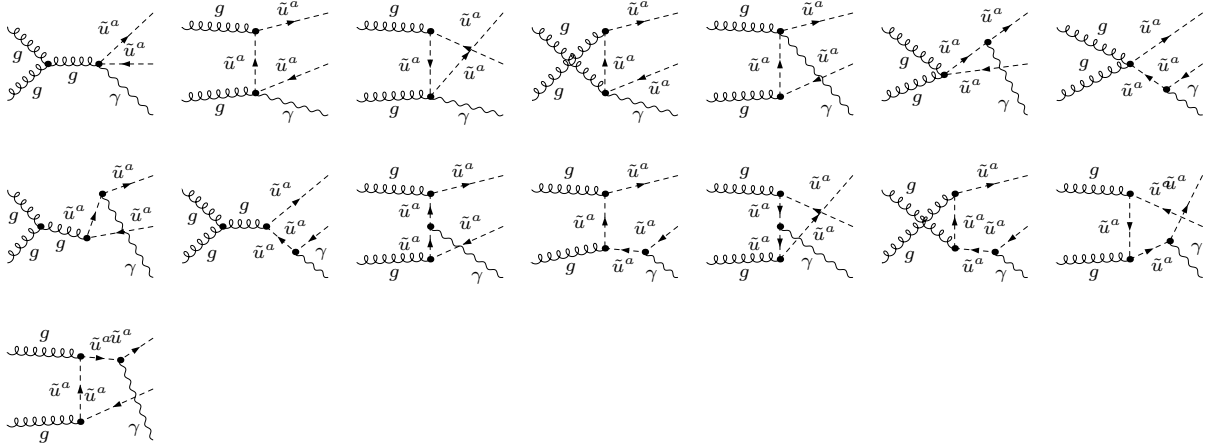


Figure 4: Tree-level diagrams for real photon emission in $gg \rightarrow \tilde{u}^a \tilde{u}^{a*} \gamma$.

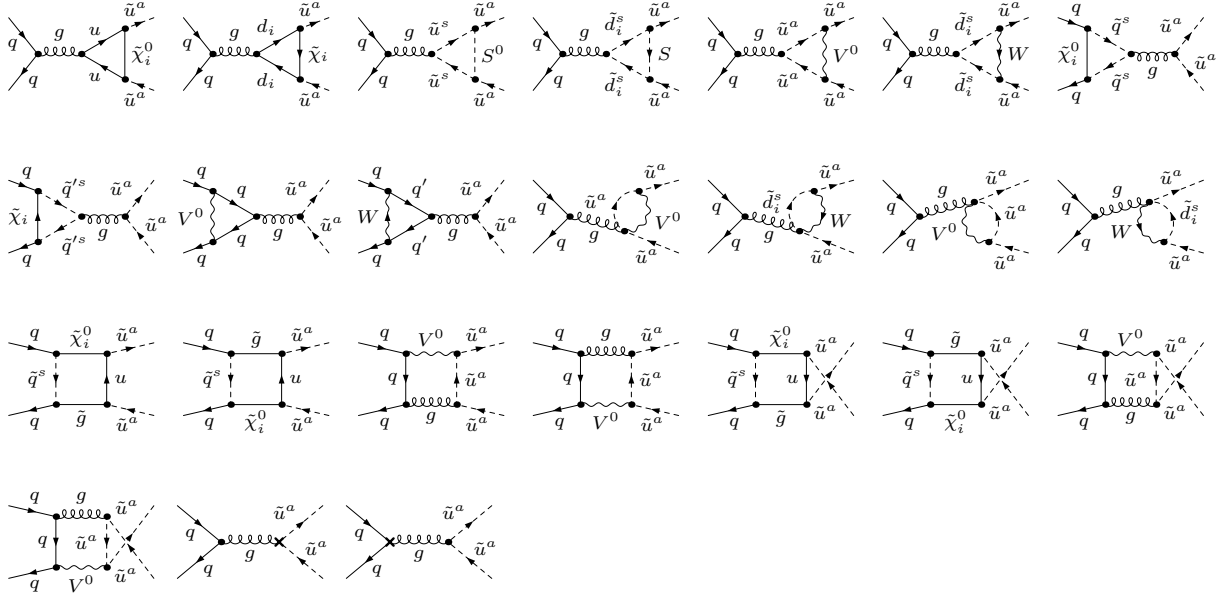


Figure 5: One-loop EW diagrams for $q\bar{q} \rightarrow \tilde{u}^a \tilde{u}^{a*}$. The diagrams with counter terms can be computed according to the Feynman rules in appendix B. The renormalization constants in the counter terms have to be evaluated at $\mathcal{O}(\alpha)$.

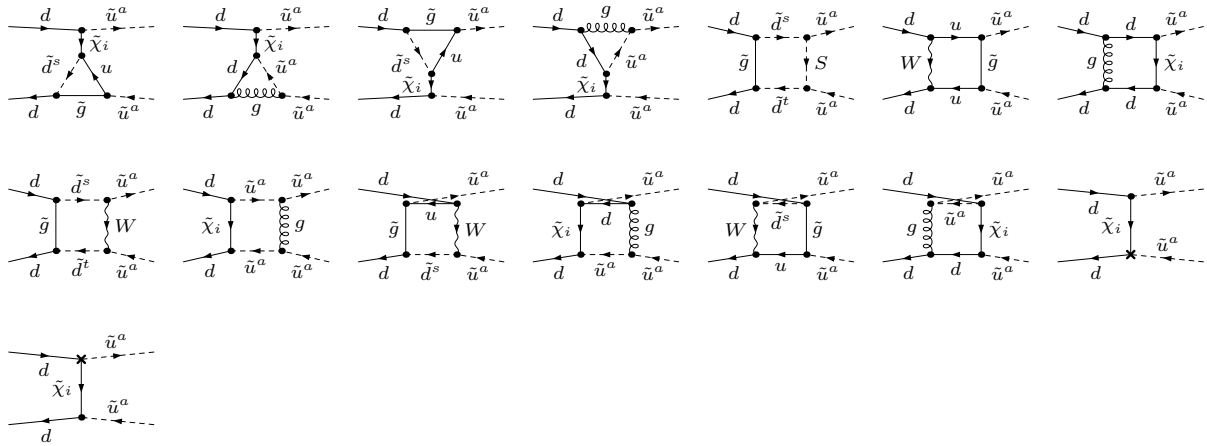


Figure 6: One-loop EW diagrams that enter only in the case of the process $d\bar{d} \rightarrow \tilde{u}^a \tilde{u}^{a*}$. The diagrams containing the counter terms can be computed according to the Feynman rules in Appendix B. The renormalization constants in the counter terms have to be evaluated at $\mathcal{O}(\alpha_s)$.

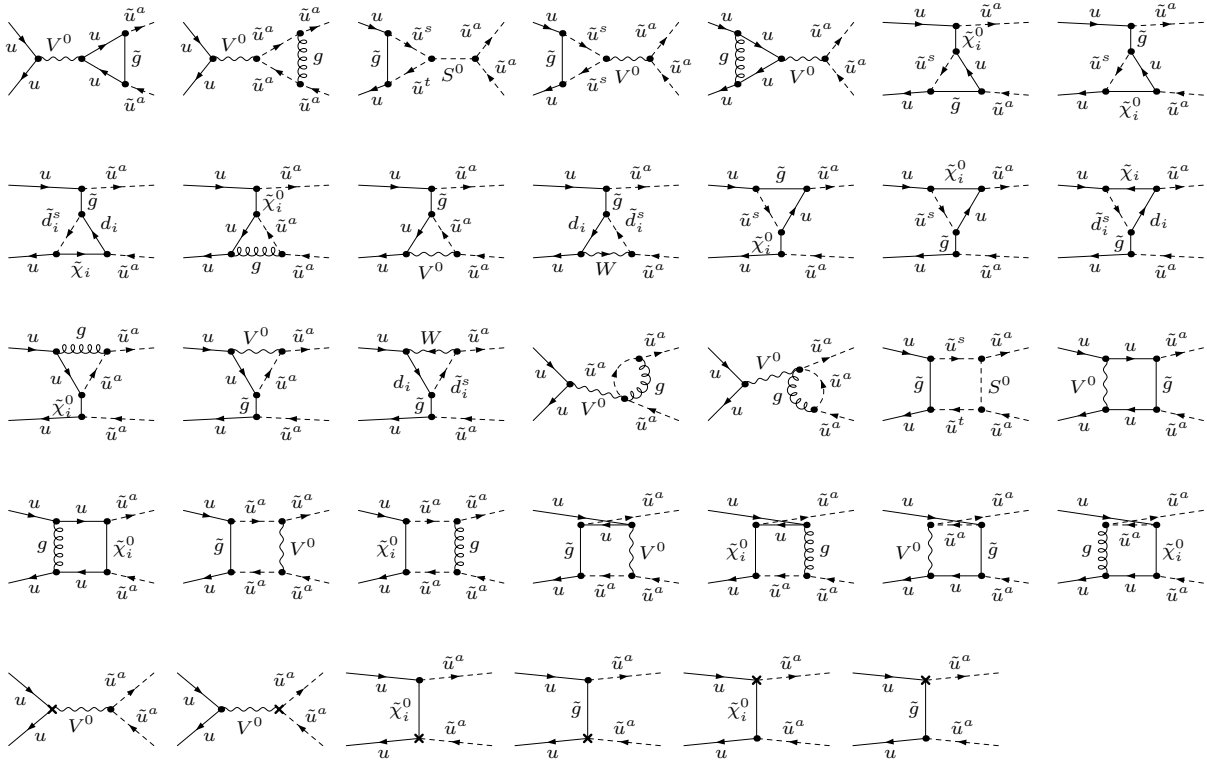


Figure 7: One-loop EW diagrams that enter only in the case of the process $u\bar{u} \rightarrow \tilde{u}^a\tilde{u}^{a*}$. The diagrams in the last row contain the counter terms listed in Appendix B. The renormalization constants in the quark–squark–gluino counter term have to be evaluated at $\mathcal{O}(\alpha)$, the other ones at $\mathcal{O}(\alpha_s)$.

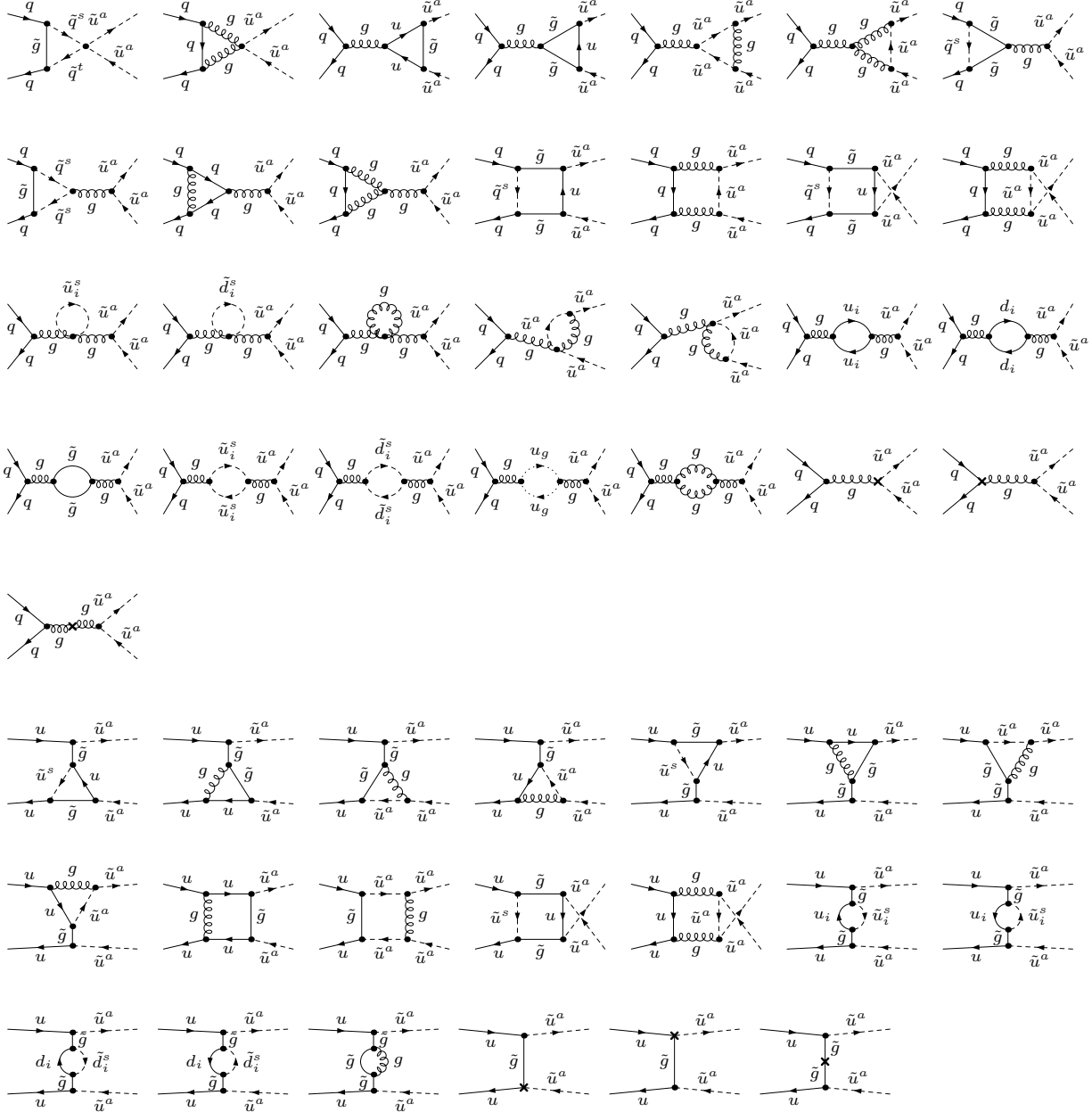


Figure 8: One loop QCD diagrams for the process $q\bar{q} \rightarrow \tilde{u}^a \tilde{u}^{a*}$. These diagrams interfere with those of Fig. 2 yielding $\mathcal{O}(\alpha_s^2 \alpha)$ contributions. The diagrams containing counter terms can be computed according to the Feynman rules listed in Appendix B. The renormalization constants appearing in the counter terms have to be evaluated at $\mathcal{O}(\alpha_s)$.

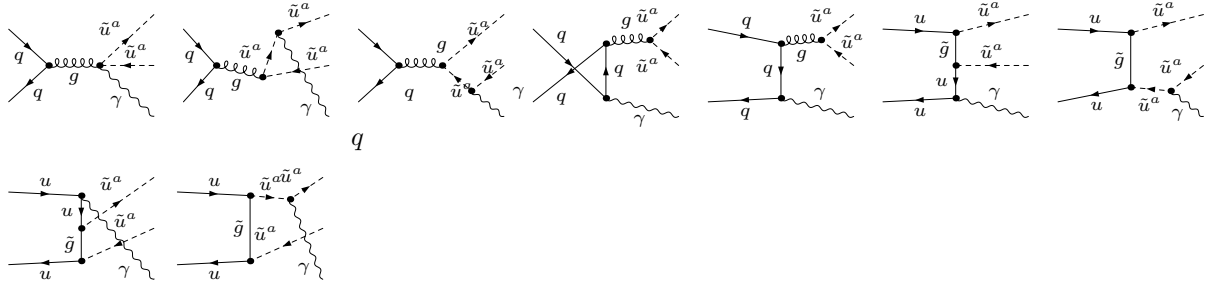


Figure 9: $\mathcal{O}(\alpha_s^2\alpha)$ real photon emission in $q\bar{q} \rightarrow \tilde{u}^a\tilde{u}^{a*}\gamma$. The last four diagrams contribute only if $q = u$.

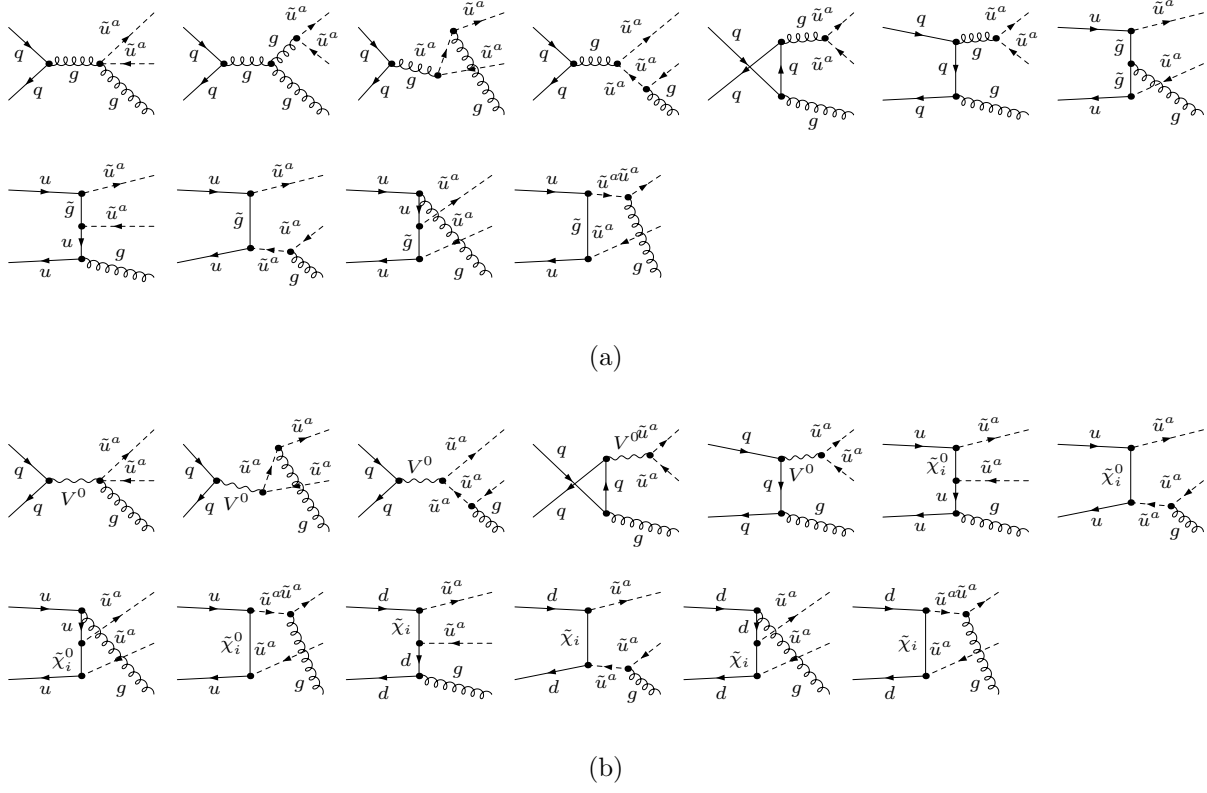


Figure 10: Diagrams for gluon bremsstrahlung from QCD (a) and EW (b) Born diagrams. They contribute at $\mathcal{O}(\alpha_s^2\alpha)$ through QCD–EW interference

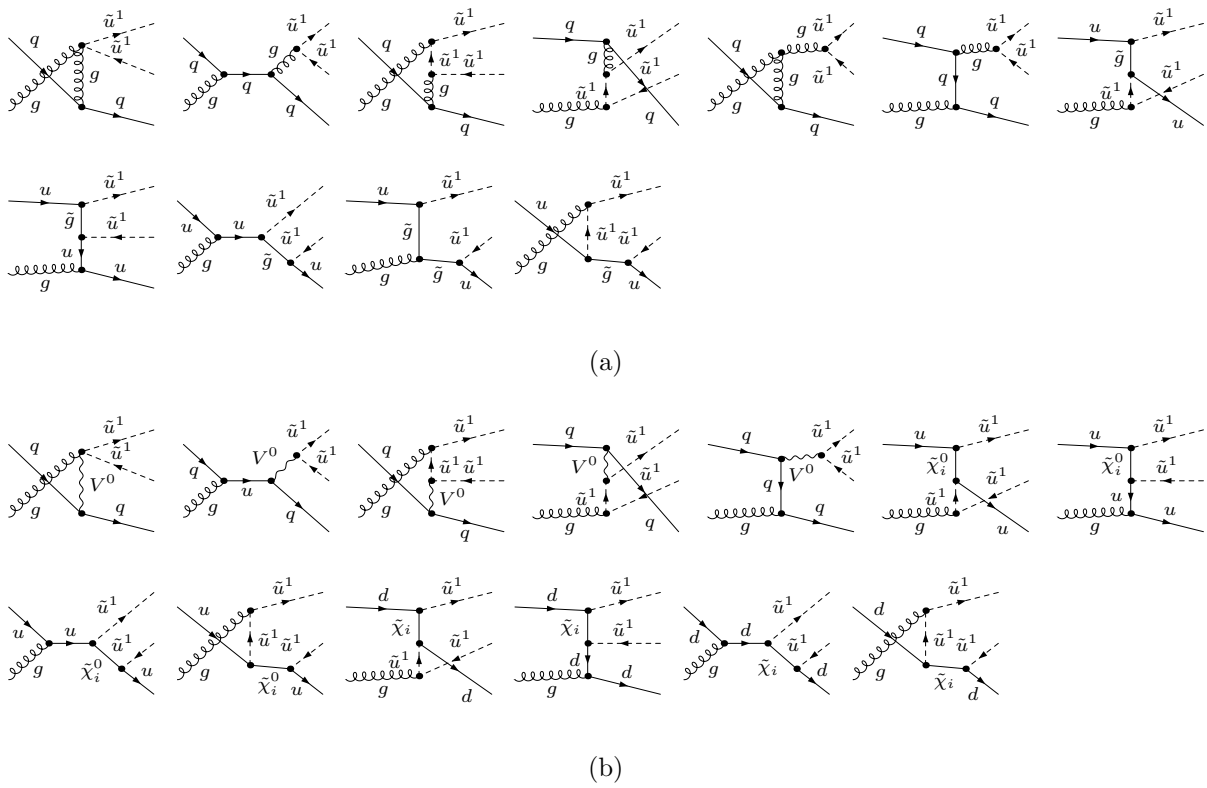


Figure 11: QCD (a) and EW (b) Born diagrams for quark gluon fusion channels. Their interference contributes at $\mathcal{O}(\alpha_s^2\alpha)$.

B Counter terms and renormalization constants

Here we list the counter terms for renormalization of vertices and propagators in the one-loop amplitudes for squark-pair production. For squarks of the first two generations, we can neglect L - R mixing, and weak eigenstates are also mass eigenstates that can be distinguished by their chiralities $a = L, R$. The Feynman rules for the counter terms can be expressed in terms of the field renormalization constants of quarks, squarks, gluons, and gluinos, defined from the relation between bare and renormalized fields,

$$\begin{aligned}\Psi_{qa}^{\text{bare}} &= \Psi_{qa}^{\text{ren}} \left(1 + \frac{1}{2} \delta Z_{qa} \right), & \Phi_{\tilde{Q},a}^{\text{bare}} &= \Phi_{\tilde{Q},a}^{\text{ren}} \left(1 + \frac{1}{2} \delta Z_{\tilde{Q},a} \right), \\ G_\mu^{\text{bare}} &= G_\mu^{\text{ren}} \left(1 + \frac{1}{2} \delta Z_G \right), & \Psi_{\tilde{g}}^{\text{bare}} &= \Psi_{\tilde{g}}^{\text{ren}} \left(1 + \frac{1}{2} \delta Z_{\tilde{g}} \right),\end{aligned}\quad (22)$$

together with the renormalization constants for the strong coupling g_s , for the strong Yukawa coupling \hat{g}_s , and for the squark masses, which are defined according to

$$g_s^{\text{bare}} = g_s^{\text{ren}} (1 + \delta Z_g), \quad \hat{g}_s^{\text{bare}} = \hat{g}_s^{\text{ren}} (1 + \delta Z_{\hat{g}}), \quad m_{\tilde{Q},a}^2{}^{\text{bare}} = m_{\tilde{Q},a}^2{}^{\text{ren}} + \delta m_{\tilde{Q},a}^2. \quad (23)$$

The actual expressions of the counterterms that are relevant for our squark-pair production processes are given below.

- Vertex counter terms involving gauge bosons:

$$\begin{aligned}\text{Diagram 1: } & \text{Wavy gluon line } g \text{ meeting a vertex } \times \text{ with two dashed squark lines } \tilde{Q}^a. & = & -ig_s(\delta Z_{\tilde{Q},a} + \frac{\delta Z_G}{2} + \delta Z_g) T^C (k+k')_\mu \\ \text{Diagram 2: } & \text{Two wavy gluon lines } g \text{ meeting a vertex } \times \text{ with two dashed squark lines } \tilde{Q}^a. & = & ig_s^2 \delta Z_{\tilde{Q},a} (\frac{1}{3} \delta C_1 C_2 + f^{C_1 C_2 A} T^A) g_{\mu\nu} \\ \text{Diagram 3: } & \text{Two solid quark lines } q \text{ meeting a vertex } \times \text{ with a wavy gluon line } g. & = & -ig_s [(\frac{\delta Z_G}{2} + \delta Z_g + \delta Z_{qL}) \gamma_\mu \omega_- + (\frac{\delta Z_G}{2} + \delta Z_g + \delta Z_{qR}) \gamma_\mu \omega_+] T^C \\ \text{Diagram 4: } & \text{Two solid quark lines } q \text{ meeting a vertex } \times \text{ with a wavy gluon line } V^0. & = & -ie [C_-^V(q) \delta Z_{qL} \gamma_\mu \omega_- + C_+^V(q) \delta Z_{qR} \gamma_\mu \omega_+] \quad V^0 = \gamma, Z \\ \text{Diagram 5: } & \text{A wavy gluon line } V^0 \text{ meeting a vertex } \times \text{ with two dashed squark lines } \tilde{Q}^a. & = & -ie [C_-^V(\tilde{Q}) \delta_{aL} + C_+^V(\tilde{Q}) \delta_{aR}] \delta Z_{\tilde{Q},a} (k+k')_\mu \quad V^0 = \gamma, Z\end{aligned}$$

k and k' are the momenta of the squark and the antisquark, and they are fixed according to the arrow. T^C are the color matrices and f^{ABC} the structure constants of the color group. We omit the color indices of fermions and sfermions. Moreover, we define

$$C_\pm^V(q) = e_q, \quad C_-^Z(q) = \frac{1}{c_W s_W} (I_q^3 - e_q s_W^2), \quad C_+^Z(q) = -\frac{s_W}{c_W} e_q, \quad (24)$$

where s_W and c_W are sine and cosine of the electroweak mixing angle θ_W .

- Self energy counter terms:

$$\begin{array}{c} \text{---} \xrightarrow{\tilde{Q}^a} \text{---} \\ \times \\ \text{---} \xrightarrow{\tilde{Q}^a} \text{---} \end{array} = i[(p^2 - m_{\tilde{Q},a}^2)\delta Z_{\tilde{Q},a} - \delta m_{\tilde{Q},a}^2]$$

$$\begin{array}{c} \text{---} \\ \times \\ \text{---} \end{array} \begin{array}{c} \tilde{g} \\ \tilde{g} \end{array} = i[(\not{p} - m_{\tilde{g}})\delta Z_{\tilde{g}} - \delta m_{\tilde{g}}]$$

$$\begin{array}{c} \text{---} \\ \times \\ \text{---} \end{array} \begin{array}{c} g \\ g \end{array} = i(p_\mu p_\nu - g_{\mu\nu} p^2)\delta Z_G$$

- Vertex counter terms involving gauginos:

$$\begin{array}{c} \text{---} \xrightarrow{Q} \times \begin{array}{c} \tilde{g} \\ \tilde{Q}^a \end{array} \end{array} = -i\frac{g_s}{\sqrt{2}} [(\delta Z_{\tilde{Q},a} + 2\delta Z_{\tilde{g}} + \delta Z_{\tilde{g}} + \delta Z_{QL}) \delta_{aL} \omega_- - (\delta Z_{\tilde{Q},a} + 2\delta Z_{\tilde{g}} + \delta Z_{\tilde{g}} + \delta Z_{QR}) \delta_{aR} \omega_+] T^C$$

$$\begin{array}{c} \text{---} \xleftarrow{Q} \times \begin{array}{c} \tilde{g} \\ \tilde{Q}^a \end{array} \end{array} = i\frac{g_s}{\sqrt{2}} [(\delta Z_{\tilde{Q},a} + 2\delta Z_{\tilde{g}} + \delta Z_{\tilde{g}} + \delta Z_{QR}) \delta_{aR} \omega_- - (\delta Z_{\tilde{Q},a} + 2\delta Z_{\tilde{g}} + \delta Z_{\tilde{g}} + \delta Z_{QL}) \delta_{aL} \omega_+] T^C$$

$$\begin{array}{c} \text{---} \xrightarrow{Q} \times \begin{array}{c} \tilde{\chi}_i^0 \\ \tilde{Q}^a \end{array} \end{array} = ie[A_-(Q) (\delta Z_{\tilde{Q},a} + \delta Z_{QL})\delta_{aL} \omega_- + A_+(Q) (\delta Z_{\tilde{Q},a} + \delta Z_{QR})\delta_{aR} \omega_+]$$

$$\begin{array}{c} \text{---} \xleftarrow{Q} \times \begin{array}{c} \tilde{\chi}_i^0 \\ \tilde{Q}^a \end{array} \end{array} = ie[A_+^*(Q) (\delta Z_{\tilde{Q},a} + \delta Z_{QR})\delta_{aR} \omega_- + A_-^*(Q) (\delta Z_{\tilde{Q},a} + \delta Z_{QL})\delta_{aL} \omega_+]$$

$$\begin{array}{c} \text{---} \xrightarrow{Q'} \times \begin{array}{c} \tilde{\chi}_i \\ \tilde{Q}^a \end{array} \end{array} = -ie\frac{B(Q')}{2s_W} (\delta Z_{\tilde{Q},a} + \delta Z_{Q'L})\delta_{aL} \omega_-$$

$$\begin{array}{c} \text{---} \xleftarrow{Q'} \times \begin{array}{c} \tilde{\chi}_i \\ \tilde{Q}^a \end{array} \end{array} = -ie\frac{B^*(Q')}{2s_W} (\delta Z_{\tilde{Q},a} + \delta Z_{Q'L})\delta_{aL} \omega_+$$

The Feynman rules involving Majorana particles follow the prescription of Ref. [67]; in particular the fermion flow is fixed according to the arrow depicted in the quark line. As usual, Q' denotes

the $SU(2)$ partner of Q . The vertices involving neutralinos contain the quantities

$$A_+(Q) = \frac{1}{\sqrt{2}} \frac{e_Q N_{i1}}{c_W}, \quad A_-(Q) = -\frac{1}{\sqrt{2}} \left(\frac{1}{6} \frac{N_{i1}^*}{c_W} + I_Q \frac{N_{i2}^*}{s_W} \right), \quad (25)$$

where N_{ij} is the mixing matrix of the neutralinos. $B(Q')$ can be expressed in terms of the mixing matrices U and V of the chargino sector: $B(Q') = U_{i1}^*$ [$B(Q') = V_{i1}^*$] for up [down] type quarks.

The renormalization constants of the squark sector are fixed by on-shell conditions (see also Ref. [34,44]),

$$\begin{aligned} \delta Z_{\tilde{Q},a} &= -\Re \left\{ \frac{\partial \Sigma_{\tilde{Q},a}(p^2)}{\partial p^2} \right\}_{|p^2=m_{\tilde{Q},a}^2}, & \delta m_{\tilde{Q},a}^2 &= \Re \left\{ \Sigma_{\tilde{Q},a}(m_{\tilde{Q},a}^2) \right\}, \\ \delta Z_{\tilde{Q}',a} &= -\Re \left\{ \frac{\partial \Sigma_{\tilde{Q}',a}(p^2)}{\partial p^2} \right\}_{|p^2=m_{\tilde{Q}',a}^2}, & \delta m_{\tilde{Q}',R}^2 &= \Re \left\{ \Sigma_{\tilde{Q}',R}(m_{\tilde{Q}',R}^2) \right\}, \end{aligned} \quad (26)$$

where (\tilde{Q}, \tilde{Q}') is either of the two $SU(2)$ doublets $(\tilde{u}, \tilde{d}), (\tilde{c}, \tilde{s})$, and $\Sigma_{\tilde{Q},a}$ is the self energy of the squark \tilde{Q}^a . Due to $SU(2)$ invariance the mass counter term of the left-handed down-type squark is a dependent quantity,

$$\delta m_{\tilde{Q}',L}^2 = \delta m_{\tilde{Q},L}^2 - c_{2\beta} \delta M_W^2 + 4M_W^2 c_\beta^3 s_\beta \delta t_\beta, \quad (27)$$

(where $c_\theta = \cos \theta$, $s_\theta = \sin \theta$ etc. for abbreviation). The counter term δt_β for $\tan \beta$ is fixed in the $\overline{\text{DR}}$ scheme and can be written in the following way [68,69],

$$\delta t_\beta = \frac{1}{2M_Z c_\beta^2} \Re \left\{ \Sigma_{A^0 Z}^{\text{div}}(m_{A^0}^2) \right\}, \quad (28)$$

where Σ^{div} denotes the divergent part of the $A^0 Z$ self energy in dimensional reduction. As pointed out in [70], this process-independent condition is also gauge invariant. Furthermore, the W mass counter term appears in (28), in the on-shell scheme given by

$$\delta M_W^2 = \Re \left\{ \Sigma_W^T(M_W^2) \right\}, \quad (29)$$

where Σ_W^T is the transverse part of the W self energy.

The field renormalization constants of the quarks are obtained via on-shell conditions as follows [71],

$$\delta Z_{qa} = -\Re \left\{ \Sigma_{qa}(m_q^2) \right\} - m_q^2 \Re \left\{ \frac{\partial}{\partial p^2} (\Sigma_{qL}(p^2) + \Sigma_{qR}(p^2) + 2\Sigma_{qS}(p^2)) \right\}_{|p^2=m_q^2} \quad (a = L, R) \quad (30)$$

with the scalar coefficients in the Lorentz decomposition of the self energy,

$$\Sigma_q(p^2) = \not{p} \omega_- \Sigma_{qL}(p^2) + \not{p} \omega_+ \Sigma_{qR}(p^2) + m_q \Sigma_{qS}(p^2). \quad (31)$$

Also in the gluino sector we determine the renormalization constants by on-shell conditions,

$$\begin{aligned} \delta m_{\tilde{g}} &= \frac{1}{2} \Re \left\{ m_{\tilde{g}} (\Sigma_{\tilde{g}L}(m_{\tilde{g}}^2) + \Sigma_{\tilde{g}R}(m_{\tilde{g}}^2) + 2\Sigma_{\tilde{g}S}(m_{\tilde{g}}^2)) \right\} \\ \delta Z_{\tilde{g}} &= -\Re \left\{ \Sigma_{\tilde{g}L}(m_{\tilde{g}}^2) \right\} - m_{\tilde{g}}^2 \Re \left\{ \frac{\partial}{\partial p^2} (\Sigma_{\tilde{g}L}(p^2) + \Sigma_{\tilde{g}R}(p^2) + 2\Sigma_{\tilde{g}S}(p^2)) \right\}_{|p^2=m_{\tilde{g}}^2}. \end{aligned} \quad (32)$$

The renormalization of the strong coupling deserves some particular care. As mentioned in Section 3.3 the strong coupling g_s is renormalized in the $\overline{\text{MS}}$ scheme decoupling the heavy particles (top, gluino and squarks) from its running. Accordingly, the renormalization constant for g_s in (23) is given by [24]

$$\delta Z_g = -\frac{\alpha_s}{4\pi} \left[\frac{3}{2} \Delta + \ln \left(\frac{m_{\tilde{g}}^2}{\mu^2} \right) + \sum_{\tilde{Q},a} \frac{1}{12} \ln \left(\frac{m_{\tilde{Q},a}^2}{\mu^2} \right) + \frac{1}{3} \ln \left(\frac{m_t^2}{\mu^2} \right) \right] \quad (33)$$

where $\Delta = 2/\epsilon - \gamma_E + \ln(4\pi)$. The treatment of UV divergences in dimensional regularization violates supersymmetry at the one-loop level, introducing a mismatch between the strong Yukawa coupling and g_s . In order to restore supersymmetry in physical amplitudes, cancellation of this extra term is required, which at one-loop order can be achieved by modifying the renormalization constant for \hat{g}_s to be different from δZ_g :

$$\delta Z_{\hat{g}} = \delta Z_g + \frac{\alpha_s}{3\pi}. \quad (34)$$

For completeness we quote also the field renormalization constant of the gluon in Eq. (22),

$$\delta Z_G = 2\delta Z_g. \quad (35)$$

At $\mathcal{O}(\alpha_s^2)$ it enters only the one-loop amplitude $\mathcal{M}_{q\bar{q} \rightarrow \tilde{Q}^a \tilde{Q}^{a*}}^{1,\text{qed}}$, but since the gluon only appears in internal lines, δZ_G is cancelled in the sum of self energy and vertex counter terms.

C Bremsstrahlung integrals

Here we list the IR and collinearly singular integrals that appear in the phase space integration of the bremsstrahlung processes, with either photons or gluons radiated. In the phase space slicing method, cuts are imposed: $\Delta E = 2\delta_s \sqrt{s}$ on the energy of the emitted photon (gluon), and an angle cut δ_c on the angle between the photon/gluon and the radiating quark via $\cos \theta > 1 - \delta_c$. The phase space is thus split into a soft and a collinear region that are singular and a complementary non-singular region, which is integrated numerically.

The integration over the soft region can be performed analytically, regularizing the singularities by small masses for the photon (gluon) and the light quarks. With the help of explicit formulae for the IR integrals [71, 72], one obtains the factorized expressions for the cross section given below. In the collinear region, the integration can be expressed as a convolution of the lowest-order cross section and a radiator function.

Process $gg \rightarrow \tilde{Q}^a \tilde{Q}^{a*} \gamma$

This process is affected by IR singularities only. Integrated over the soft region, the differential cross section reads as follows,

$$d\sigma_{gg \rightarrow \tilde{Q}^a \tilde{Q}^{a*} \gamma}^{2,1} = -\frac{\alpha}{\pi} e_{\tilde{Q}}^2 (\delta_F - \delta_{FF}) d\sigma_{gg \rightarrow \tilde{Q}^a \tilde{Q}^{a*}}^{2,0} \quad (36)$$

where

$$\begin{aligned} \delta_F &= \ln\left(\frac{4\Delta E^2}{\lambda^2}\right) + \frac{1}{\beta} \ln\left(\frac{1-\beta}{1+\beta}\right) \\ \delta_{FF} &= \frac{2}{\beta} \left(\frac{s - 2m_{\tilde{Q},a}^2}{s}\right) \left[\frac{1}{2} \ln\left(\frac{1+\beta}{1-\beta}\right) \ln\left(\frac{4\Delta E^2}{\lambda^2}\right) - \text{Li}_2\left(\frac{2\beta}{1+\beta}\right) - \frac{1}{4} \ln^2\left(\frac{1+\beta}{1-\beta}\right) \right]. \end{aligned}$$

λ is the infinitesimal mass regularizing the IR divergencies, and $\beta = \sqrt{1 - (4m_{\tilde{Q},a}^2/s)}$.

Process $q\bar{q} \rightarrow \tilde{Q}^a \tilde{Q}^{a*} \gamma$

The differential cross section integrated over the soft region can be expressed in terms of the $\mathcal{O}(\alpha_s^2)$ cross section for $q\bar{q} \rightarrow \tilde{Q}^a \tilde{Q}^{a*}$ and a IR-singular factor,

$$d\sigma_{q\bar{q} \rightarrow \tilde{Q}^a \tilde{Q}^{a*} \gamma}^{2,1} = -\frac{\alpha}{\pi} \left[e_q^2 (\delta_I - \delta_{II}) + e_{\tilde{Q}}^2 (\delta_F - \delta_{FF}) + e_q e_{\tilde{Q}} (\delta_{IF} - \delta_{FI}) \right] d\sigma_{q\bar{q} \rightarrow \tilde{Q}^a \tilde{Q}^{a*}}^{2,0} \quad (37)$$

where $e_q = \frac{2}{3}$ if $q = u, c$ and $e_q = -\frac{1}{3}$ otherwise. Furthermore,

$$\begin{aligned}
\delta_I &= \ln\left(\frac{4\Delta E^2}{\lambda^2}\right) + \ln\left(\frac{m_q^2}{s}\right), \\
\delta_{II} &= \ln\left(\frac{s}{m_q^2}\right) \ln\left(\frac{4\Delta E^2}{\lambda^2}\right) - \frac{\pi^2}{3} - \frac{1}{2} \ln^2\left(\frac{s}{m_q^2}\right), \\
\delta_{IF} &= \ln\left(\frac{m_q^2 m_{\tilde{Q},a}^2}{(t - m_{\tilde{Q},a}^2)^2}\right) \ln\left(\frac{4\Delta E^2}{\lambda^2}\right) + \frac{1}{2} \left[\ln^2\left(\frac{m_q^2}{s}\right) - \ln^2\left(\frac{1-\beta}{1+\beta}\right) \right] + \frac{\pi^2}{3} + 2\text{Li}_2\left(1 + \frac{st}{(m_{\tilde{Q},a}^2 - t)^2}\right) \\
&\quad - 2 \left[\text{Li}_2\left(1 + \frac{(1-\beta)st}{2m_{\tilde{Q},a}^2(m_{\tilde{Q},a}^2 - t)}\right) + \text{Li}_2\left(1 + \frac{(1+\beta)st}{2m_{\tilde{Q},a}^2(m_{\tilde{Q},a}^2 - t)}\right) \right];
\end{aligned} \tag{38}$$

δ_{FI} can be obtained from δ_{IF} by the substitution $t \rightarrow u$.

The differential cross section integrated over the collinear region can be written in terms of a convolution integral,

$$d\sigma_{q\bar{q} \rightarrow \tilde{Q}^a \tilde{Q}^{a*} \gamma}^{2,1}(s) = \frac{\alpha e_q^2}{2\pi} \int_{x_0}^{1-\delta_s} dz \left\{ \left[\ln\left(\frac{s\delta_c}{2m_q^2}\right) - 1 \right] P_{qq}(z) + (1-z) \right\} d\sigma_{q\bar{q} \rightarrow \tilde{Q}^a \tilde{Q}^{a*}}^{2,0}(zs), \tag{39}$$

with $x_0 = (4m_{\tilde{Q},a}^2)/s$ and the quark splitting function $P_{qq}(z)$ from Eq. (18).

Process $q\bar{q} \rightarrow \tilde{Q}^a \tilde{Q}^{a*} g$

The singularities affecting this radiative process are Abelian-like, similar to the case of photon radiation, and thus can be treated by mass regularization as well. The differential cross section integrated over the soft region can also be expressed in terms of $\mathcal{O}(\alpha_s \alpha)$ contributions to the cross section for $q\bar{q} \rightarrow \tilde{Q}^a \tilde{Q}^{a*}$, but only together with a rearrangement of the color structure. The emission of a gluon as a colored particle leads to color correlations in the eikonal current, which can be taken into account following the prescription of Ref. [48], yielding the result

$$\begin{aligned}
d\sigma_{q\bar{q} \rightarrow \tilde{Q}^a \tilde{Q}^{a*} g}^{2,1} &= -\frac{\alpha_s}{2\pi} \left\{ \left[C_F (2\delta_I + 2\delta_F) + 2 \left(C_F + \frac{1}{N} \right) \delta_{FI} + \frac{1}{N} (\delta_{II} + \delta_{FF} - \delta_{IF}) \right] d\bar{\sigma}_{q\bar{q} \rightarrow \tilde{Q}^a \tilde{Q}^{a*}}^{1,1} \right. \\
&\quad \left. - \left[\delta_{FI} - \delta_{IF} \right] d\bar{\sigma}_{q\bar{q} \rightarrow \tilde{Q}^a \tilde{Q}^{a*}}^{1,1} - \left[\delta_{FI} + \delta_{II} + \delta_{FF} \right] d\bar{\sigma}_{q\bar{q} \rightarrow \tilde{Q}^a \tilde{Q}^{a*}}^{1,1} \right\},
\end{aligned} \tag{40}$$

with $C_F = \frac{4}{3}$ and $N = 3$. In order to specify the color-modified ‘‘cross sections’’ $d\bar{\sigma}$ and $d\tilde{\sigma}$, we first separate the tree-level amplitudes for $q\bar{q} \rightarrow \tilde{Q}^a \tilde{Q}^{a*}$ into color factors and reduced matrix elements, according to the s - and t -channel diagrams in Fig. 1:

$$\begin{aligned}
\mathcal{M}_{q\bar{q} \rightarrow \tilde{Q}^a \tilde{Q}^{a*}}^{0,\text{qcd} [c_1, c_2, c_3, c_4]} &= \sum_C \left(T_{c_2 c_1}^C T_{c_3 c_4}^C \mathcal{M}_{q\bar{q} \rightarrow \tilde{Q}^a \tilde{Q}^{a*}}^{0,\text{qcd} (s)} + T_{c_3 c_1}^C T_{c_2 c_4}^C \mathcal{M}_{q\bar{q} \rightarrow \tilde{Q}^a \tilde{Q}^{a*}}^{0,\text{qcd} (t)} \right), \\
\mathcal{M}_{q\bar{q} \rightarrow \tilde{Q}^a \tilde{Q}^{a*}}^{0,\text{ew} [c_1, c_2, c_3, c_4]} &= \delta_{c_1 c_2} \delta_{c_3 c_4} \mathcal{M}_{q\bar{q} \rightarrow \tilde{Q}^a \tilde{Q}^{a*}}^{0,\text{ew} (s)} + \delta_{c_1 c_3} \delta_{c_2 c_4} \mathcal{M}_{q\bar{q} \rightarrow \tilde{Q}^a \tilde{Q}^{a*}}^{0,\text{ew} (t)}
\end{aligned} \tag{41}$$

where T^C are the color matrices in the fundamental representation. With this notation we can write for the color-rearranged contributions,

$$\begin{aligned}
d\bar{\sigma}_{q\bar{q} \rightarrow \tilde{Q}^a \tilde{Q}^{a*}}^{-1,1} &= \frac{dt}{16\pi s^2} \frac{1}{N^2} 2 \Re \left\{ \left(\mathcal{M}_{q\bar{q} \rightarrow \tilde{Q}^a \tilde{Q}^{a*}}^{0,\text{qcd} [c_1, c_2, c_1, c_3]} \right)^* \mathcal{M}_{q\bar{q} \rightarrow \tilde{Q}^a \tilde{Q}^{a*}}^{0,\text{ew} [c_4, c_2, c_4, c_3]} \right\}, \\
d\tilde{\sigma}_{q\bar{q} \rightarrow \tilde{Q}^a \tilde{Q}^{a*}}^{-1,1} &= \frac{dt}{16\pi s^2} \frac{1}{N^2} 2 \Re \left\{ \left(\mathcal{M}_{q\bar{q} \rightarrow \tilde{Q}^a \tilde{Q}^{a*}}^{0,\text{qcd} [c_1, c_1, c_2, c_3]} \right)^* \mathcal{M}_{q\bar{q} \rightarrow \tilde{Q}^a \tilde{Q}^{a*}}^{0,\text{ew} [c_4, c_4, c_2, c_3]} \right\},
\end{aligned} \tag{42}$$

where color summation has to be performed over each pair of equal indices. On top, average over the initial helicities is assumed. Owing to the particular color structure, $d\tilde{\sigma}$ is different from zero only if $q = Q$.

The differential cross section integrated over the collinear region can be written in terms of a convolution integral similar to Eq. (39),

$$d\sigma_{q\bar{q} \rightarrow \tilde{Q}^a \tilde{Q}^{a*} g}^{2,1}(s) = \frac{\alpha_s C_F}{2\pi} \int_{x_0}^{1-\delta_s} dz \left\{ \left[\ln \left(\frac{s\delta_c}{2m_q^2} \right) - 1 \right] P_{qq}(z) + (1-z) \right\} d\sigma_{q\bar{q} \rightarrow \tilde{Q}^a \tilde{Q}^{a*}}^{1,1}(zs), \quad (43)$$

with $d\sigma_{q\bar{q} \rightarrow \tilde{Q}^a \tilde{Q}^{a*}}^{1,1}$ instead of $d\sigma_{q\bar{q} \rightarrow \tilde{Q}^a \tilde{Q}^{a*}}^{2,0}$.

Processes $qg \rightarrow \tilde{Q}^a \tilde{Q}^{a*} q$ and $\bar{q}g \rightarrow \tilde{Q}^a \tilde{Q}^{a*} \bar{q}$

These processes exhibit singularities when the final (anti-)quark is emitted off the gluon in the collinear region. In that region the differential cross section can be written, in analogy to [54], as follows,

$$\begin{aligned} d\sigma_{qg \rightarrow \tilde{Q}^a \tilde{Q}^{a*} q}^{2,1}(s) &= \frac{\alpha_s T_F}{2\pi} \int_{x_0}^1 dz \left\{ \ln \left(\frac{s(1-z)^2 \delta_c}{2m_q^2} \right) P_{qg}(z) + 2z(1-z) \right\} d\sigma_{q\bar{q} \rightarrow \tilde{Q}^a \tilde{Q}^{a*}}^{1,1}(zs) \\ d\sigma_{\bar{q}g \rightarrow \tilde{Q}^a \tilde{Q}^{a*} \bar{q}}^{2,1}(s) &= \frac{\alpha_s T_F}{2\pi} \int_{x_0}^1 dz \left\{ \ln \left(\frac{s(1-z)^2 \delta_c}{2m_q^2} \right) P_{qg}(z) + 2z(1-z) \right\} d\sigma_{q\bar{q} \rightarrow \tilde{Q}^a \tilde{Q}^{a*}}^{1,1}(zs) \end{aligned} \quad (44)$$

with the splitting function P_{qg} from Eq. (18).

References

- [1] J. Wess and B. Zumino, *Supergauge Transformations in Four-Dimensions*, *Nucl. Phys.* **B70** (1974) 39–50.
- [2] D. V. Volkov and V. P. Akulov, *Is the Neutrino a Goldstone Particle?*, *Phys. Lett.* **B46** (1973) 109–110.
- [3] H. P. Nilles, *Supersymmetry, Supergravity and Particle Physics*, *Phys. Rept.* **110** (1984) 1–162.
- [4] H. E. Haber and G. L. Kane, *The Search for Supersymmetry: Probing Physics Beyond the Standard Model*, *Phys. Rept.* **117** (1985) 75–263.
- [5] R. Barbieri, *Looking Beyond the Standard Model: The Supersymmetric Option*, *Riv. Nuovo Cim.* **11N4** (1988) 1–45.
- [6] S. Heinemeyer, W. Hollik, and G. Weiglein, *Electroweak precision observables in the minimal supersymmetric standard model*, *Phys. Rept.* **425** (2006) 265–368, [[hep-ph/0412214](#)].
- [7] J. R. Ellis, S. Heinemeyer, K. A. Olive, A. M. Weber, and G. Weiglein, *The Supersymmetric Parameter Space in Light of B-physics Observables and Electroweak Precision Data*, *JHEP* **08** (2007) 083, [[arXiv:0706.0652](#)].
- [8] O. Buchmueller *et. al.*, *Prediction for the Lightest Higgs Boson Mass in the CMSSM using Indirect Experimental Constraints*, *Phys. Lett.* **B657** (2007) 87–94, [[arXiv:0707.3447](#)].
- [9] **Muon g-2** Collaboration, G. W. Bennett *et. al.*, *Measurement of the positive muon anomalous magnetic moment to 0.7-ppm*, *Phys. Rev. Lett.* **89** (2002) 101804, [[hep-ex/0208001](#)].
- [10] **Muon g-2** Collaboration, G. W. Bennett *et. al.*, *Measurement of the negative muon anomalous magnetic moment to 0.7-ppm*, *Phys. Rev. Lett.* **92** (2004) 161802, [[hep-ex/0401008](#)].
- [11] LEP Collaborations and LEP Electroweak Working Group and SLD Electroweak Group and SLD Heavy Flavour Group, *Precision electroweak measurements on the Z resonance*, *Phys. Rept.* **427** (2006) 257, [[hep-ex/0509008](#)].
- [12] LEP Collaborations and LEP Electroweak Working Group, *A combination of preliminary electroweak measurements and constraints on the standard model*, [hep-ex/0612034](#).
- [13] M. W. Grunewald, *Combined Electroweak Analysis*, [arXiv:0709.3744](#).
- [14] T. Plehn, D. Rainwater, and P. Skands, *Squark and gluino production with jets*, *Phys. Lett.* **B645** (2007) 217–221, [[hep-ph/0510144](#)].
- [15] L. Randall and D. Tucker-Smith, *Dijet Searches for Supersymmetry at the LHC*, [arXiv:0806.1049](#).
- [16] **LHC/LC Study Group** Collaboration, G. Weiglein *et. al.*, *Physics interplay of the LHC and the ILC*, *Phys. Rept.* **426** (2006) 47–358, [[hep-ph/0410364](#)].
- [17] **ATLAS** Collaboration, A. Tricomi, *Particle reconstruction at LHC*, [hep-ex/0406020](#).
- [18] M. Chiorboli and A. Tricomi, *Squark and gluino reconstruction in CMS*, . CMS-NOTE-2004-029.
- [19] P. R. Harrison and C. H. Llewellyn Smith, *Hadroproduction of Supersymmetric Particles*, *Nucl. Phys.* **B213** (1983) 223.
- [20] G. L. Kane and J. P. Leveille, *Experimental Constraints on Gluino Masses and Supersymmetric Theories*, *Phys. Lett.* **B112** (1982) 227.

- [21] E. Reya and D. P. Roy, *Supersymmetric particle production at p anti- p collider energies*, *Phys. Rev.* **D32** (1985) 645.
- [22] S. Dawson, E. Eichten, and C. Quigg, *Search for Supersymmetric Particles in Hadron - Hadron Collisions*, *Phys. Rev.* **D31** (1985) 1581.
- [23] H. Baer and X. Tata, *Component formulae for hadronproduction of left-handed and right-handed squarks*, *Phys. Lett.* **B160** (1985) 159.
- [24] W. Beenakker, R. Hopker, M. Spira, and P. M. Zerwas, *Squark and gluino production at hadron colliders*, *Nucl. Phys.* **B492** (1997) 51–103, [[hep-ph/9610490](#)].
- [25] W. Beenakker, R. Hopker, and M. Spira, *PROSPINO: A program for the PROduction of Supersymmetric Particles In Next-to-leading Order QCD*, [hep-ph/9611232](#).
- [26] W. Beenakker, M. Kramer, T. Plehn, M. Spira, and P. M. Zerwas, *Stop production at hadron colliders*, *Nucl. Phys.* **B515** (1998) 3–14, [[hep-ph/9710451](#)].
- [27] S. Bornhauser, M. Drees, H. K. Dreiner, and J. S. Kim, *Electroweak Contributions to Squark Pair Production at the LHC*, *Phys. Rev.* **D76** (2007) 095020, [[arXiv:0709.2544](#)].
- [28] G. Bozzi, B. Fuks, and M. Klasen, *Non-diagonal and mixed squark production at hadron colliders*, *Phys. Rev.* **D72** (2005) 035016, [[hep-ph/0507073](#)].
- [29] W. Hollik, M. Kollar, and M. K. Trenkel, *EW NLO corrections to pair production of top-squarks at the LHC*, [arXiv:0710.2472](#).
- [30] W. Hollik, M. Kollar, and M. K. Trenkel, *Hadronic production of top-squark pairs with electroweak NLO contributions*, *JHEP* **02** (2008) 018, [[arXiv:0712.0287](#)].
- [31] M. Beccaria, G. Macorini, L. Panizzi, F. M. Renard, and C. Verzegnassi, *Stop-antistop and sbottom-antisbottom production at LHC: a one-loop search for model parameters dependence*, [arXiv:0804.1252](#).
- [32] F. E. Paige, *SUSY signatures in ATLAS at LHC*, [hep-ph/0307342](#).
- [33] K. Kawagoe, M. M. Nojiri, and G. Polesello, *A new SUSY mass reconstruction method at the CERN LHC*, *Phys. Rev.* **D71** (2005) 035008, [[hep-ph/0410160](#)].
- [34] S. Heinemeyer, W. Hollik, H. Rzehak, and G. Weiglein, *High-precision predictions for the MSSM Higgs sector at $O(\alpha_b\alpha_s)$* , *Eur. Phys. J.* **C39** (2005) 465–481, [[hep-ph/0411114](#)].
- [35] M. S. Carena, D. Garcia, U. Nierste, and C. E. M. Wagner, *Effective Lagrangian for the anti- t b H^+ interaction in the MSSM and charged Higgs phenomenology*, *Nucl. Phys.* **B577** (2000) 88–120, [[hep-ph/9912516](#)].
- [36] F. I. Olness and W.-K. Tung, *When Is a Heavy Quark Not a Parton? Charged Higgs Production and Heavy Quark Mass Effects in the QCD Based Parton Model*, *Nucl. Phys.* **B308** (1988) 813.
- [37] D. Dicus, T. Stelzer, Z. Sullivan, and S. Willenbrock, *Higgs boson production in association with bottom quarks at next-to-leading order*, *Phys. Rev.* **D59** (1999) 094016, [[hep-ph/9811492](#)].
- [38] F. Maltoni, Z. Sullivan, and S. Willenbrock, *Higgs-boson production via bottom-quark fusion*, *Phys. Rev.* **D67** (2003) 093005, [[hep-ph/0301033](#)].
- [39] A. D. Martin, R. G. Roberts, W. J. Stirling, and R. S. Thorne, *Parton distributions incorporating QED contributions*, *Eur. Phys. J.* **C39** (2005) 155–161, [[hep-ph/0411040](#)].
- [40] T. Hahn, *Generating Feynman diagrams and amplitudes with FeynArts 3*, *Comput. Phys. Commun.* **140** (2001) 418–431, [[hep-ph/0012260](#)].

- [41] T. Hahn and C. Schappacher, *The implementation of the minimal supersymmetric standard model in FeynArts and FormCalc*, *Comput. Phys. Commun.* **143** (2002) 54–68, [[hep-ph/0105349](#)].
- [42] T. Hahn and M. Perez-Victoria, *Automatized one-loop calculations in four and D dimensions*, *Comput. Phys. Commun.* **118** (1999) 153–165, [[hep-ph/9807565](#)].
- [43] T. Hahn and M. Rauch, *News from FormCalc and LoopTools*, *Nucl. Phys. Proc. Suppl.* **157** (2006) 236–240, [[hep-ph/0601248](#)].
- [44] W. Hollik and H. Rzehak, *The sfermion mass spectrum of the MSSM at the one-loop level*, *Eur. Phys. J.* **C32** (2003) 127–133, [[hep-ph/0305328](#)].
- [45] S. Dittmaier, *A general approach to photon radiation off fermions*, *Nucl. Phys.* **B565** (2000) 69–122, [[hep-ph/9904440](#)].
- [46] V. N. Baier, V. S. Fadin, and V. A. Khoze, *Quasireal electron method in high-energy quantum electrodynamics*, *Nucl. Phys.* **B65** (1973) 381–396.
- [47] S. Berge, W. Hollik, W. M. Mosle, and D. Wackerroth, *SUSY QCD one-loop effects in (un)polarized top-pair production at hadron colliders*, *Phys. Rev.* **D76** (2007) 034016, [[hep-ph/0703016](#)].
- [48] S. Catani and M. H. Seymour, *A general algorithm for calculating jet cross sections in NLO QCD*, *Nucl. Phys.* **B485** (1997) 291–419, [[hep-ph/9605323](#)].
- [49] S. Catani and M. H. Seymour, *The Dipole Formalism for the Calculation of QCD Jet Cross Sections at Next-to-Leading Order*, *Phys. Lett.* **B378** (1996) 287–301, [[hep-ph/9602277](#)].
- [50] S. Catani, S. Dittmaier, M. H. Seymour, and Z. Trocsanyi, *The dipole formalism for next-to-leading order QCD calculations with massive partons*, *Nucl. Phys.* **B627** (2002) 189–265, [[hep-ph/0201036](#)].
- [51] K. P. O. Diener, S. Dittmaier, and W. Hollik, *Electroweak higher-order effects and theoretical uncertainties in deep-inelastic neutrino scattering*, *Phys. Rev.* **D72** (2005) 093002, [[hep-ph/0509084](#)].
- [52] Y. Kurihara, D. Perret-Gallix, and Y. Shimizu, *$e^+ e^- \rightarrow e^-$ anti-electron-neutrino u anti- d from LEP to linear collider energies*, *Phys. Lett.* **B349** (1995) 367–374, [[hep-ph/9412215](#)].
- [53] U. Baur, S. Keller, and D. Wackerroth, *Electroweak radiative corrections to W boson production in hadronic collisions*, *Phys. Rev.* **D59** (1999) 013002, [[hep-ph/9807417](#)].
- [54] W. Hollik, T. Kasprzik, and B. A. Kniehl, *Electroweak corrections to W -boson hadroproduction at finite transverse momentum*, *Nucl. Phys.* **B790** (2008) 138–159, [[arXiv:0707.2553](#)].
- [55] J. A. Aguilar-Saavedra *et. al.*, *Supersymmetry parameter analysis: SPA convention and project*, *Eur. Phys. J.* **C46** (2006) 43–60, [[hep-ph/0511344](#)].
- [56] B. C. Allanach *et. al.*, *The Snowmass points and slopes: Benchmarks for SUSY searches*, [hep-ph/0202233](#).
- [57] ATLAS Data Challenge 2 DC2 points. <http://paige.home.cern.ch/paige/fullsusy/romeindex.html>.
- [58] W. Porod, *SPheno, a program for calculating supersymmetric spectra, SUSY particle decays and SUSY particle production at $e^+ e^-$ colliders*, *Comput. Phys. Commun.* **153** (2003) 275–315, [[hep-ph/0301101](#)].
- [59] A. Djouadi, J.-L. Kneur, and G. Moultaka, *SuSpect: A Fortran code for the supersymmetric and Higgs particle spectrum in the MSSM*, *Comput. Phys. Commun.* **176** (2007) 426–455, [[hep-ph/0211331](#)].

- [60] **Particle Data Group** Collaboration, W. M. Yao *et. al.*, *Review of particle physics*, *J. Phys.* **G33** (2006) 1–1232.
- [61] LEP Collaborations and LEP Working Group for Higgs Boson Searches, *Search for neutral MSSM Higgs bosons at LEP*, *Eur. Phys. J.* **C47** (2006) 547–587, [[hep-ex/0602042](#)].
- [62] **ALEPH** Collaboration, R. Barate *et. al.*, *Search for supersymmetric particles in e^+e^- collisions at $s^{1/2}$ up to 202-GeV and mass limit for the lightest neutralino*, *Phys. Lett.* **B499** (2001) 67–84, [[hep-ex/0011047](#)].
- [63] **D0** Collaboration, V. M. Abazov *et. al.*, *Search for squarks and gluinos in events with jets and missing transverse energy in $p\bar{p}$ collisions at $\sqrt{s} = 1.96$ -TeV*, *Phys. Lett.* **B638** (2006) 119–127, [[hep-ex/0604029](#)].
- [64] S. Heinemeyer, W. Hollik, and G. Weiglein, *FeynHiggs: A program for the calculation of the masses of the neutral CP-even Higgs bosons in the MSSM*, *Comput. Phys. Commun.* **124** (2000) 76–89, [[hep-ph/9812320](#)].
- [65] G. Degrandi, S. Heinemeyer, W. Hollik, P. Slavich, and G. Weiglein, *Towards high-precision predictions for the MSSM Higgs sector*, *Eur. Phys. J.* **C28** (2003) 133–143, [[hep-ph/0212020](#)].
- [66] M. Frank *et. al.*, *The Higgs boson masses and mixings of the complex MSSM in the Feynman-diagrammatic approach*, *JHEP* **02** (2007) 047, [[hep-ph/0611326](#)].
- [67] A. Denner, H. Eck, O. Hahn, and J. Kublbeck, *Compact Feynman rules for Majorana fermions*, *Phys. Lett.* **B291** (1992) 278–280.
- [68] A. Dabelstein, *The One loop renormalization of the MSSM Higgs sector and its application to the neutral scalar Higgs masses*, *Z. Phys.* **C67** (1995) 495–512, [[hep-ph/9409375](#)].
- [69] M. Frank, S. Heinemeyer, W. Hollik, and G. Weiglein, *FeynHiggs1.2: Hybrid \overline{MS} / on-shell renormalization for the CP-even Higgs boson sector in the MSSM*, [hep-ph/0202166](#).
- [70] A. Freitas and D. Stockinger, *Gauge dependence and renormalization of $\tan(\beta)$ in the MSSM*, *Phys. Rev.* **D66** (2002) 095014, [[hep-ph/0205281](#)].
- [71] A. Denner, *Techniques for calculation of electroweak radiative corrections at the one loop level and results for W physics at LEP-200*, *Fortschr. Phys.* **41** (1993) 307–420, [[arXiv:0709.1075](#)].
- [72] G. 't Hooft and M. J. G. Veltman, *Scalar One Loop Integrals*, *Nucl. Phys.* **B153** (1979) 365–401.

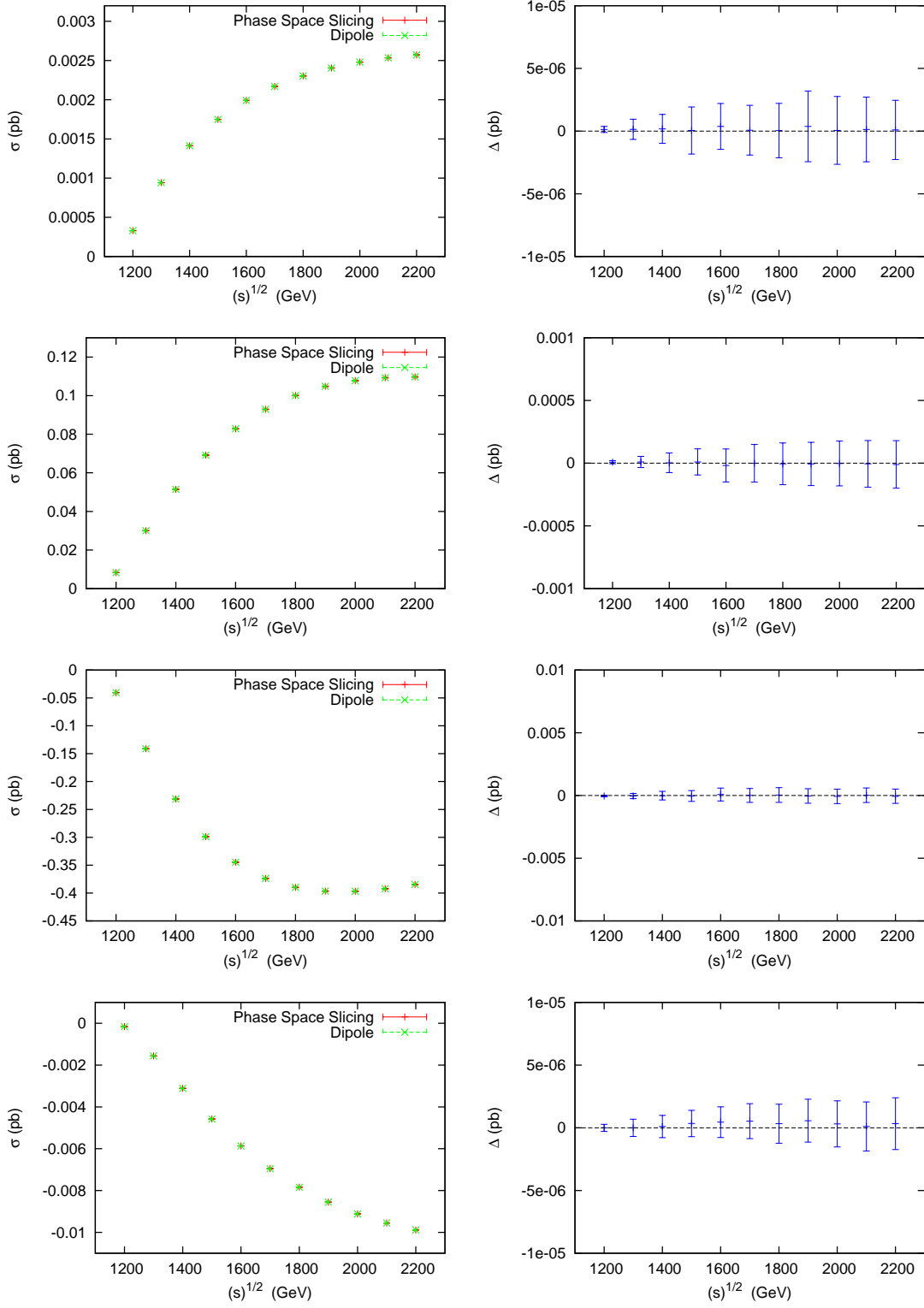


Figure 12: Lowest order partonic cross sections for the process $gg \rightarrow \tilde{u}^L \tilde{u}^{L*} \gamma$ (first panel), $u\bar{u} \rightarrow \tilde{u}^L \tilde{u}^{L*} \gamma$ (second panel), $u\bar{u} \rightarrow \tilde{u}^L \tilde{u}^{L*} g$ (third panel) and $ug \rightarrow \tilde{u}^L \tilde{u}^{L*} u$ (fourth panel), computed with the two different methods. Δ is defined as $\Delta = \sigma^{\text{Slicing}} - \sigma^{\text{Dipole}}$. The error bars represent the integration uncertainty. The SUSY parameters are those of the SPS1a' point [55].

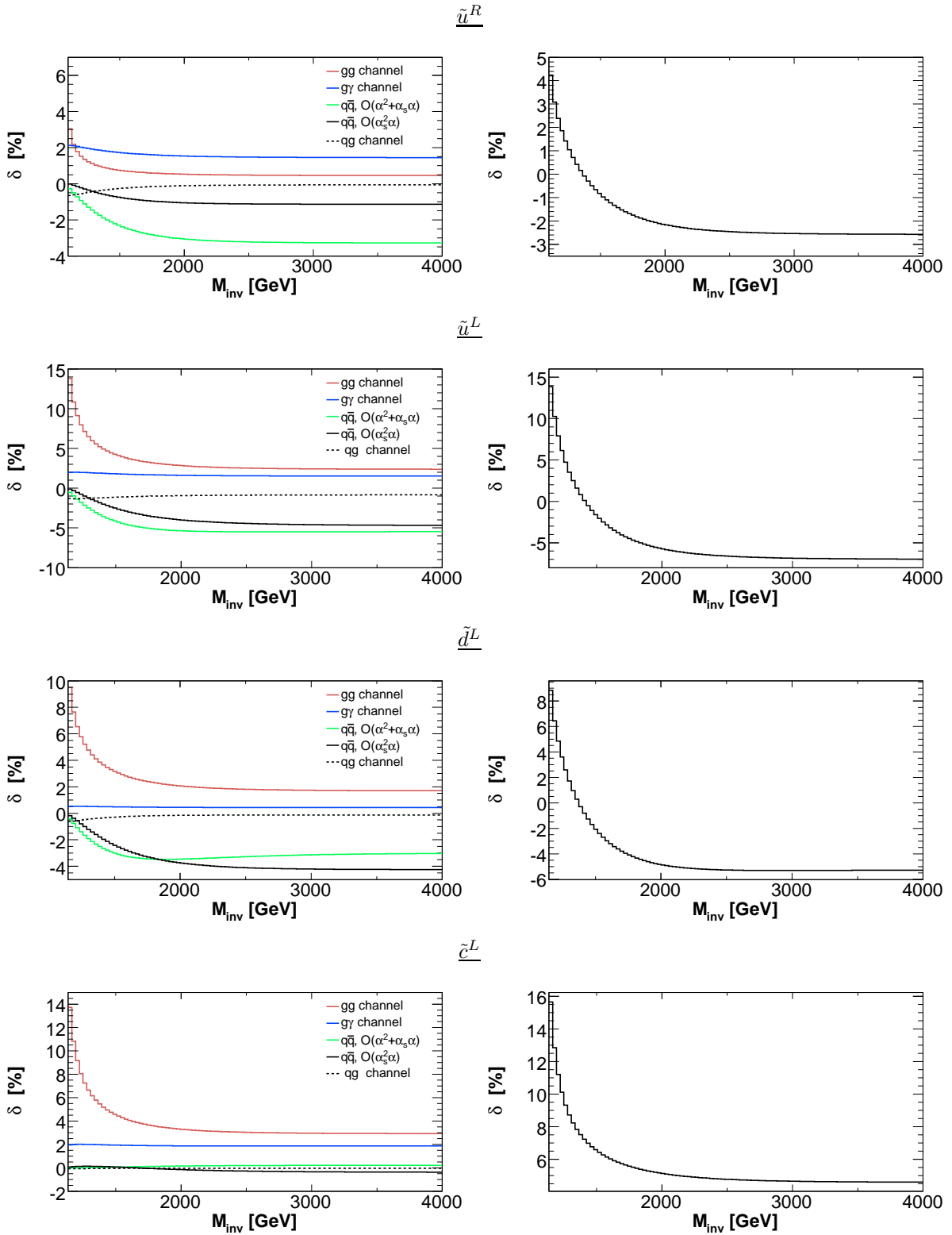


Figure 13: Cumulative invariant mass distribution for different species of squark pairs, defined as the cross section integrated up to M_{inv} of the invariant mass of the squark-antisquark pair. The left panels show the relative contributions from the various channels, the right ones show the complete EW contribution. The SUSY parameter point corresponds to SPS1a'.

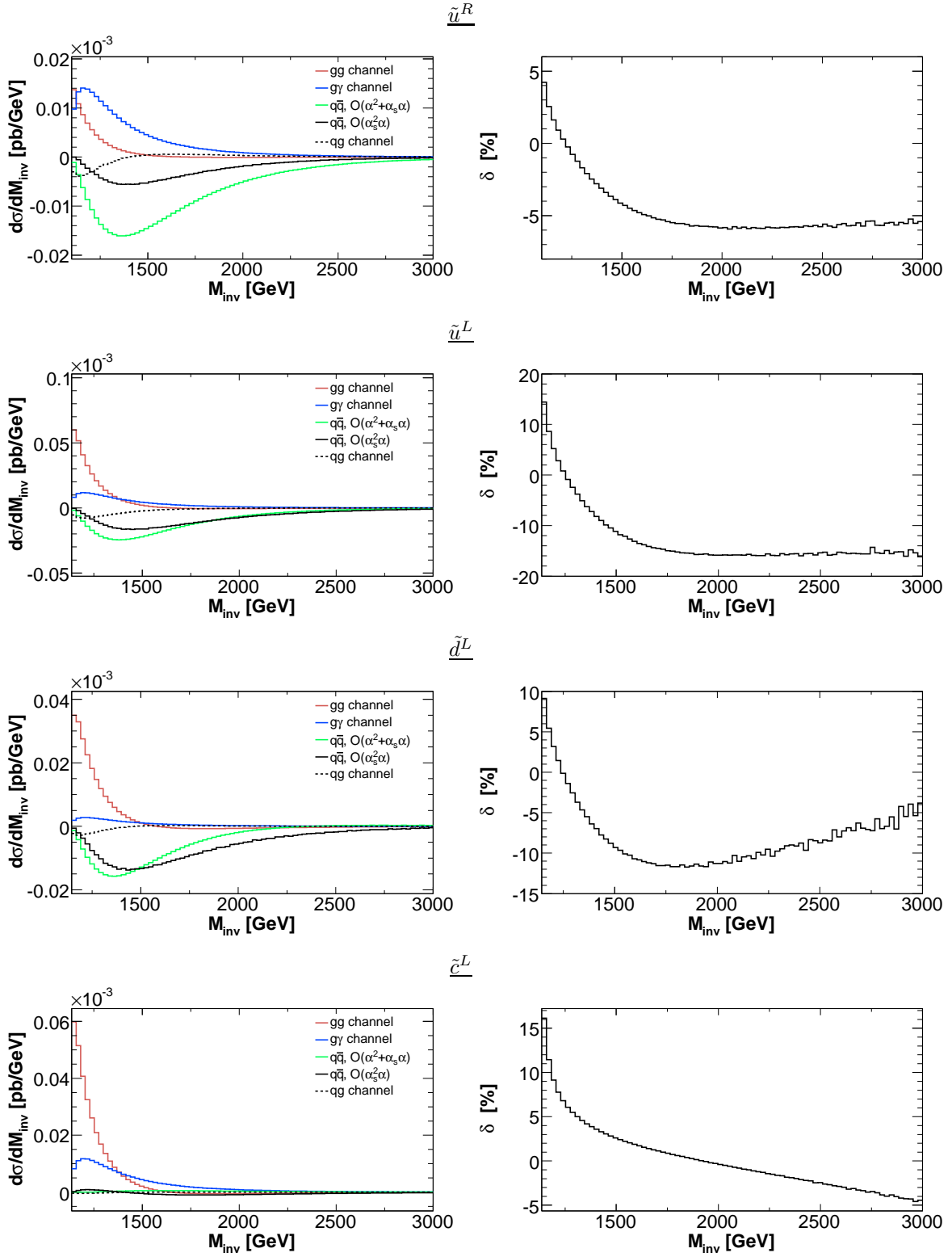


Figure 14: Invariant mass distribution for different species of squark pairs, for the SUSY parameter point corresponding to SPS1a'. The left panels show the relative contributions from the various channels, the right ones show the complete EW contribution.

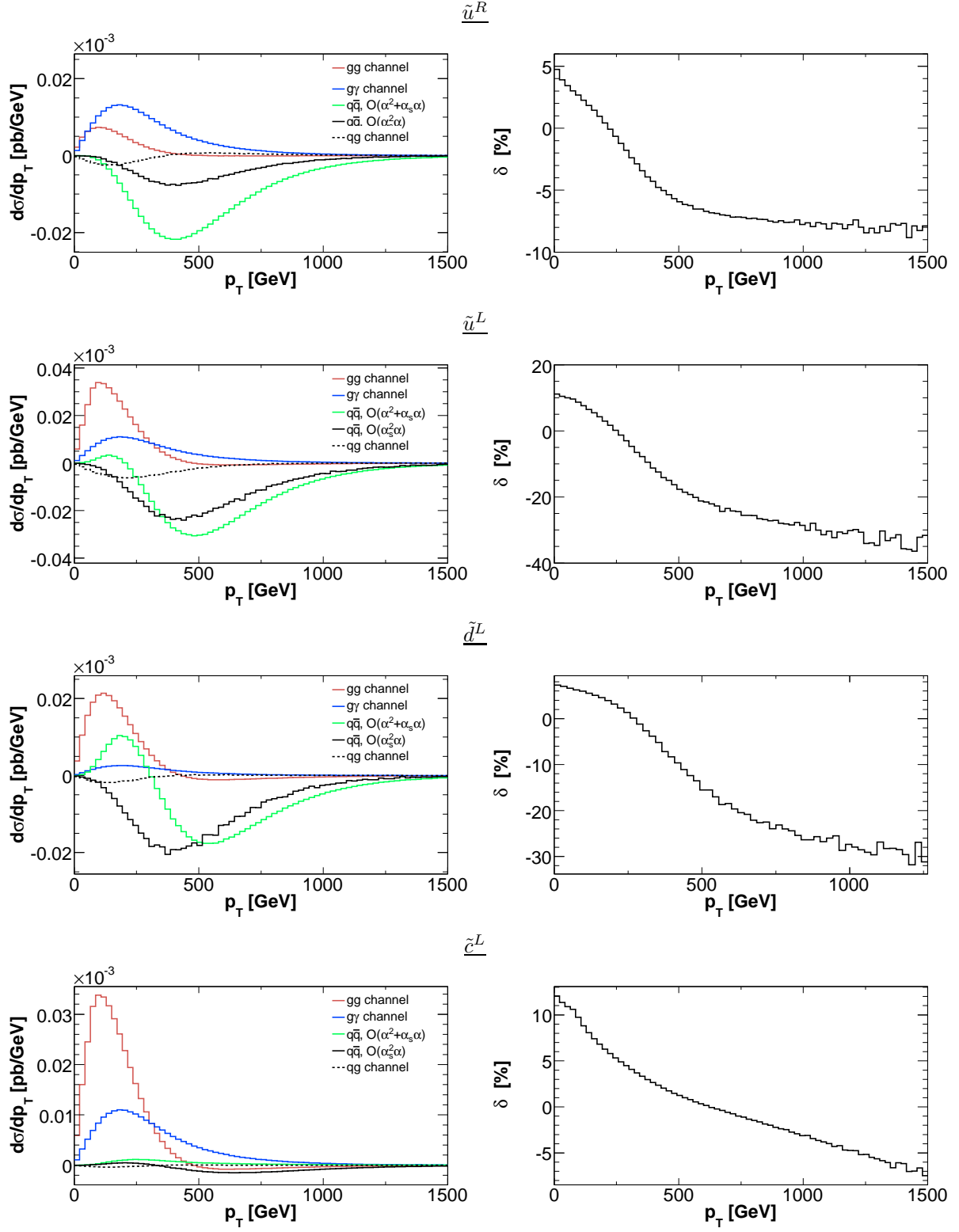


Figure 15: Transverse momentum distribution for different species of squark pairs. Notations and input parameters as in 14.

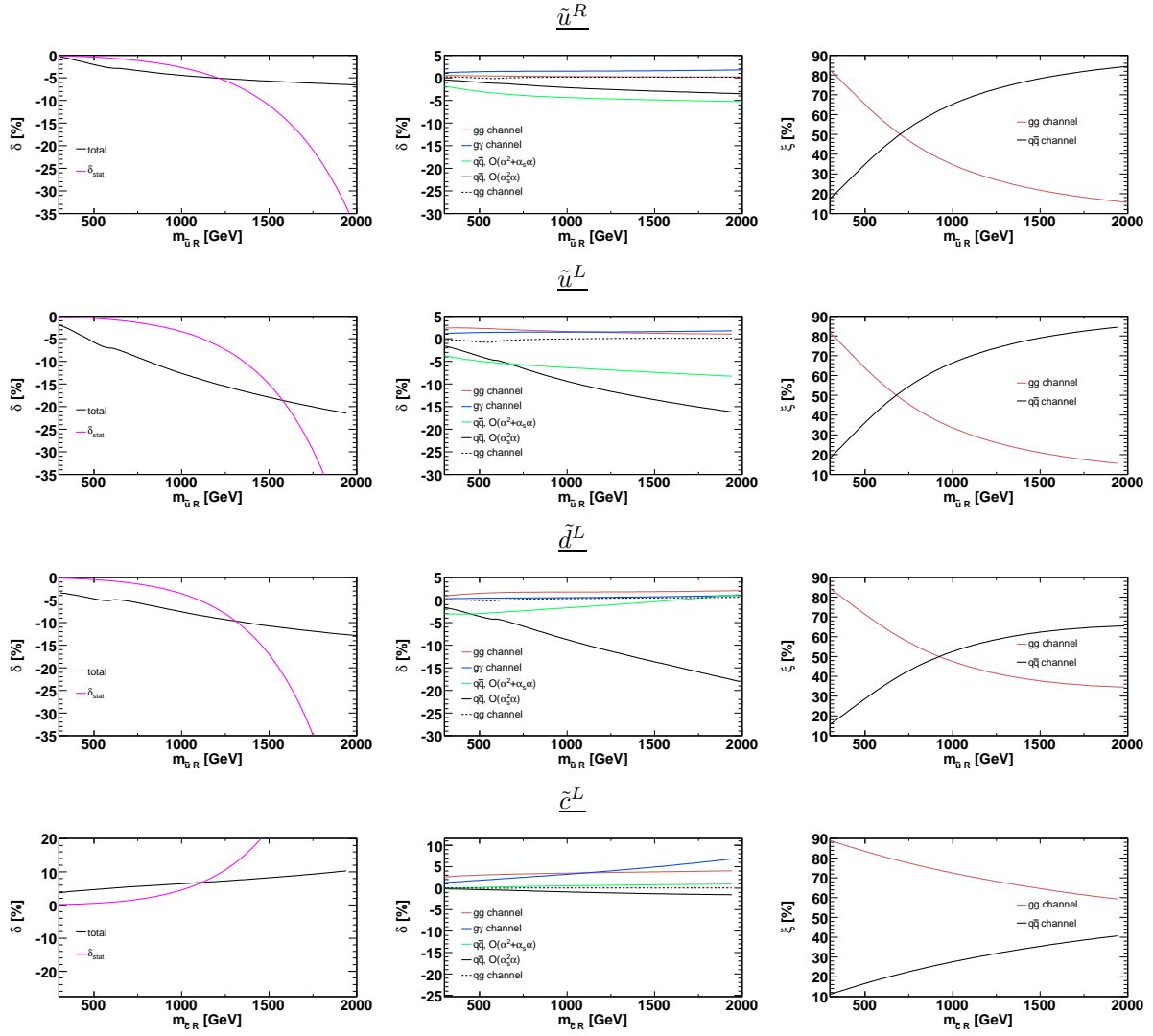


Figure 16: Squark-mass dependence of the EW contributions. Total EW contribution (left), individual contributions from the various channels (center). The panels in the right column show the relative yield of the two channels that contribute at LO.

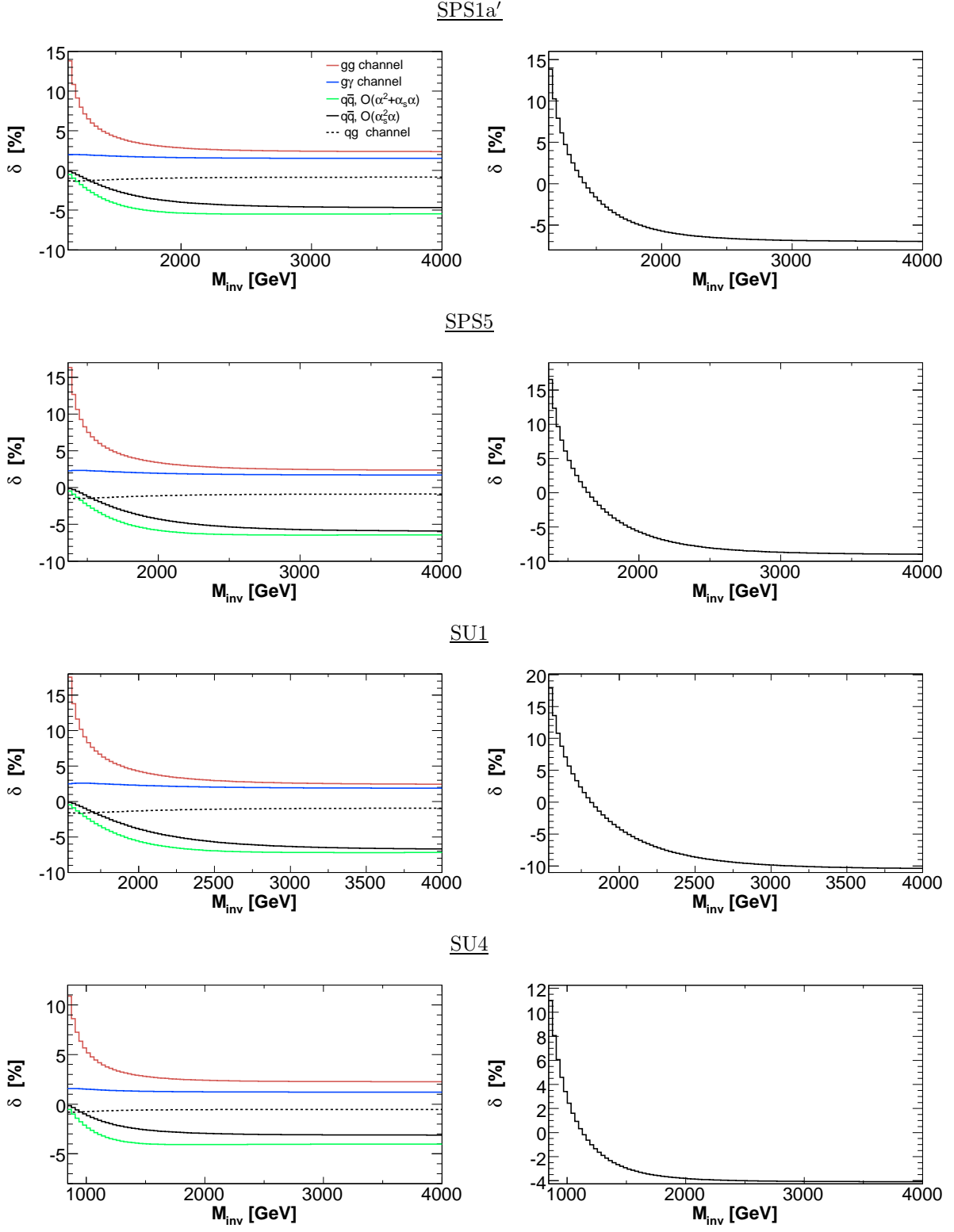


Figure 17: Cumulative invariant mass distribution for $PP \rightarrow \tilde{u}^L \tilde{u}^{L*} X$ in different SUSY scenarios. Notations as in Fig. 13.

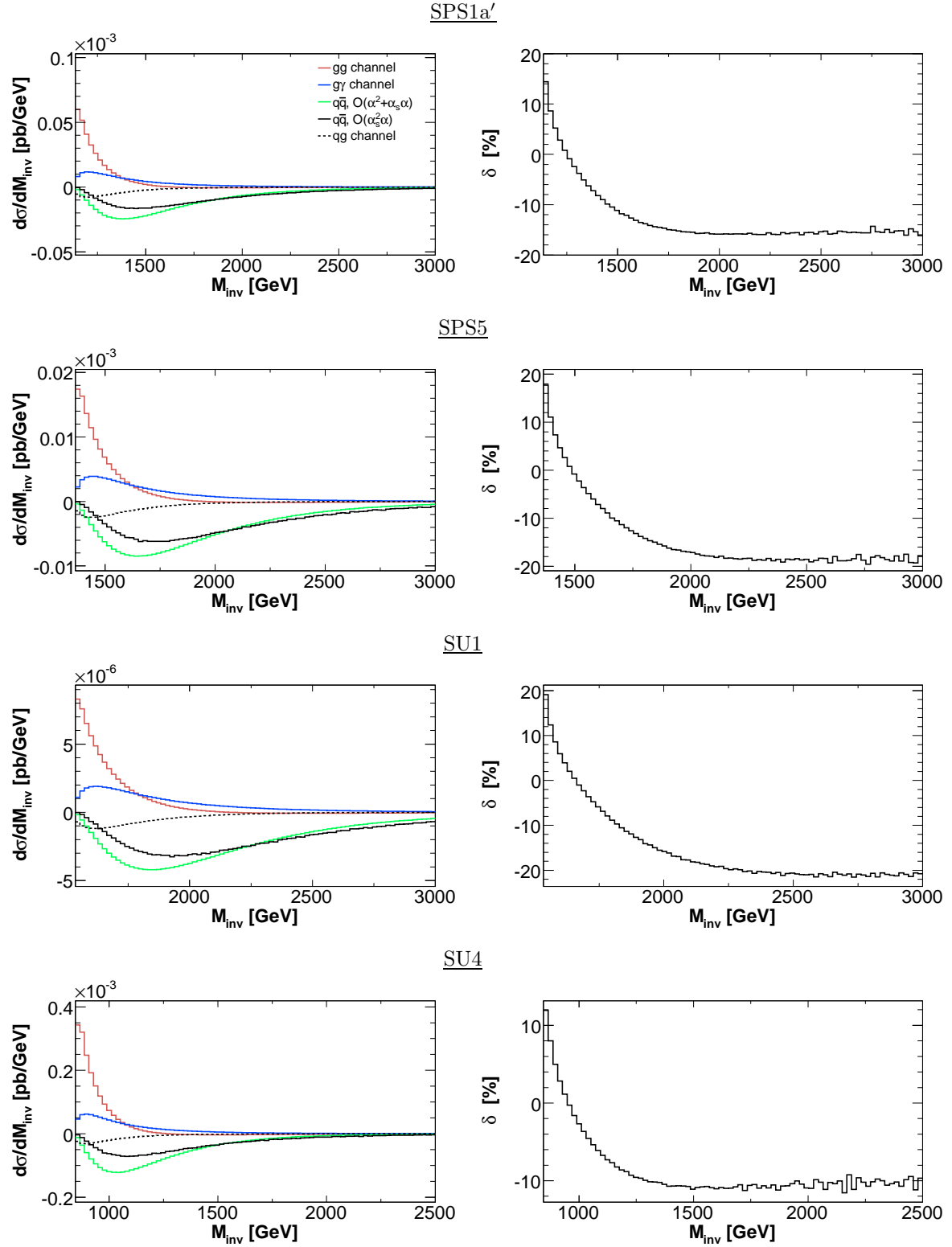


Figure 18: Invariant mass distribution for $PP \rightarrow \tilde{u}^L \tilde{u}^{L*} X$ in different SUSY scenarios. Notations as in Fig. 14.

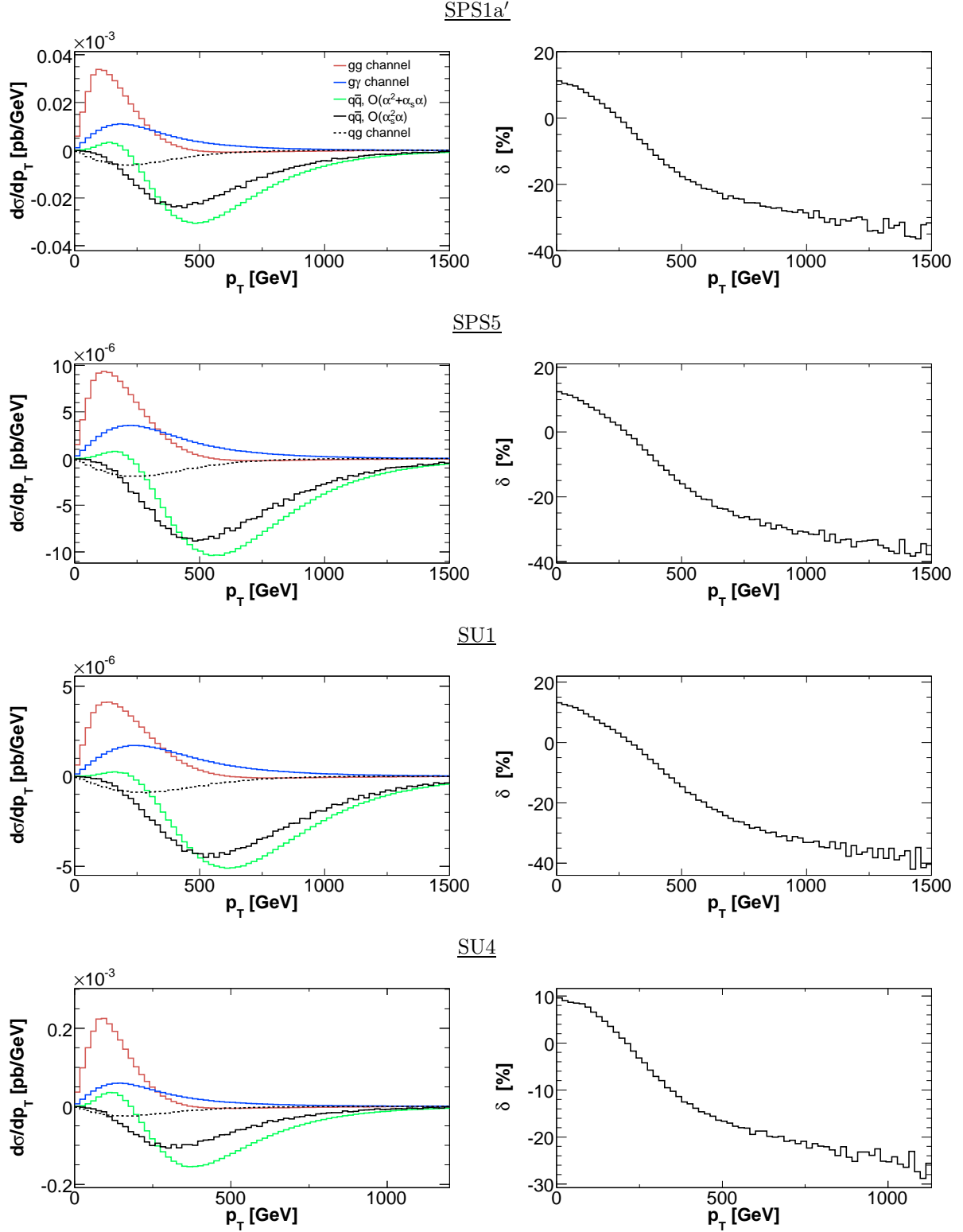


Figure 19: Transverse momentum distribution of the process $PP \rightarrow \tilde{u}^L \tilde{u}^{L*} X$ in different SUSY scenarios. Notations as in Fig. 15.

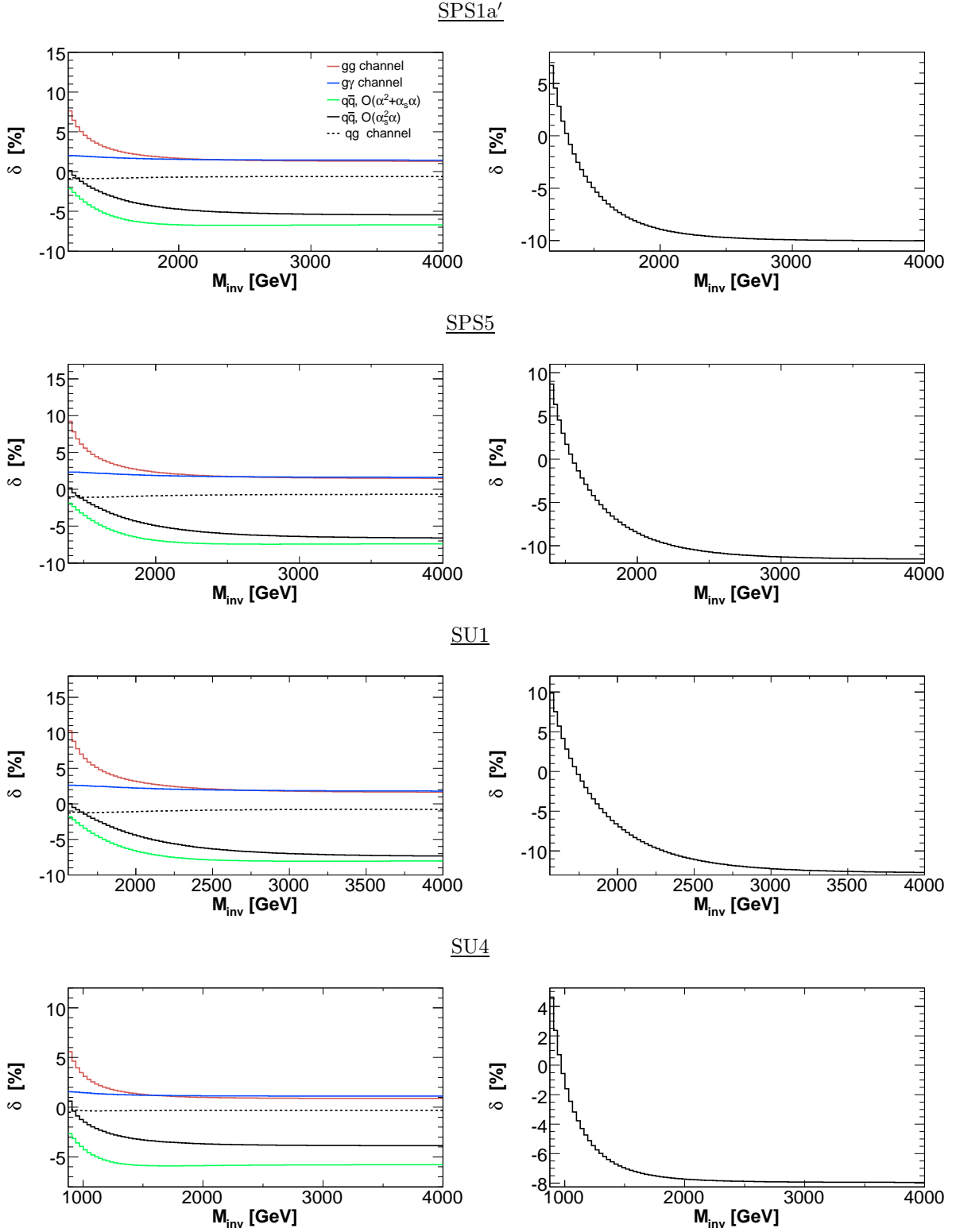


Figure 20: Same as Fig. 17, but with the kinematical cuts defined in section 4.2.

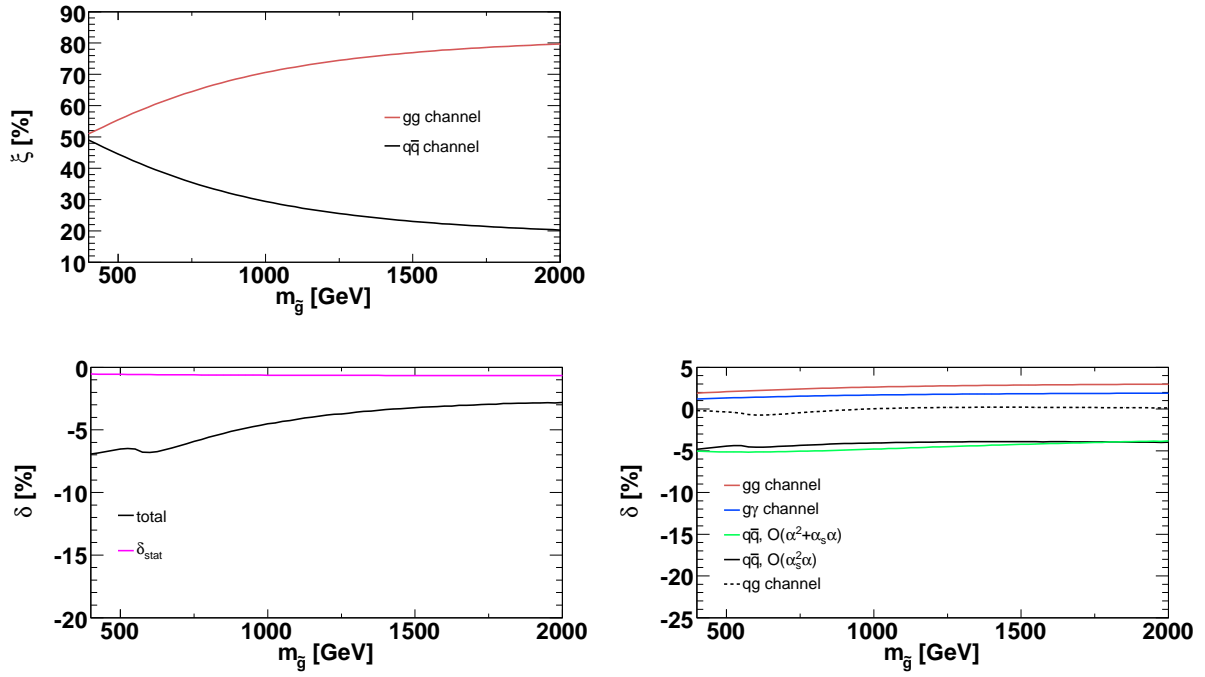


Figure 21: Gluino mass dependence of the total (lower left) and of the individual (lower right) EW contributions to the total cross section for $PP \rightarrow \hat{u}^L \hat{u}^{L*} X$. The upper panel shows the relative yield of the two channels that contribute at LO.